Geophysical Journal International

*Geophys. J. Int.* (2022) **229,** 915–932 https://doi.org/10.1093/gji/ggab476
Advance Access publication 2021 December 02
GJI Seismology

# A spectral element approach to computing normal modes

J. Kemper [1] M. van Driel [1] F. Munch [2] A. Khan [1,3] and D. Giardini [1]

[1] *Institute of Geophysics, ETH Zürich,* 8092 *Zürich, Switzerland. E-mail: johannes.kemper@erdw.ethz.ch*
[2] *Berkeley Seismological Laboratory, University of California, Berkeley, CA* 94720*, United States*
[3] *Physik-Institut, University of Zürich,* 8006 *Zürich, Switzerland*

Received 2021 November 19; in original form 2021 August 20

## SUMMARY

We introduce a new approach to the computation of gravito-elastic free oscillations or normal modes of spherically symmetric bodies based on a spectral element discretization of the radial ordinary differential equations. Our method avoids numerical instabilities often encountered in the classical method of radial integration and root finding of the characteristic function. To this end, the code is built around a sparse matrix formulation of the eigenvalue problem taking advantage of state-of-the-art parallel iterative solvers. We apply the method to toroidal, spheroidal and radial modes and we demonstrate its versatility in the presence of attenuation, fluid layers and gravity (including the purely elastic case, the Cowling approximation, and full gravity). We demonstrate higher-order convergence and verify the software by computing seismograms and comparing these to existing numerical solutions. Finally, to emphasize the general applicability of our code, we show spectra and eigenfunctions of Earth, Mars and Jupiter's icy moon Europa and discuss the different types of modes that emerge.

**Key words:** Numerical modelling; Surface waves and free oscillations; Theoretical seismology.

## 1 INTRODUCTION

The analysis of the global seismic displacement wavefield in terms of discrete frequencies termed normal modes or free oscillations is a classical approach in long-period seismology that dates back to the work of Poisson (1829), Thomson (1863) and Lamb (1881). Mathematically, the modes are described as eigenfunctions and eigenvalues of a linear operator that incorporates the elastic and gravitational forces as well as the full coupling between mass displacement and changes of the gravitational potential (Woodhouse & Deuss 2015).

Normal mode seismology has proved versatile by being able to provide information on the radial and lateral seismic structure of the Earth (e.g. Dziewonski & Anderson 1981; Woodhouse & Dziewonski 1984; Giardini *et al.* 1987; Lognonné 1991; Resovsky & Ritzwoller 1999; Al-Attar *et al.* 2012; Irving *et al.* 2018). While Earth's seismic velocity structure continues to be imaged at ever increasing resolution (e.g. French & Romanowicz 2014; Lei *et al.* 2020; Simmons *et al.* 2021), normal modes nevertheless remain the most promising means to constrain Earth's global-scale density structure (e.g. Ishii & Tromp 1999; Trampert *et al.* 2004). Yet, despite its importance in governing the dynamical evolution, Earth's density structure remains relatively poorly resolved.

The numerical calculation of the free oscillations of Earth originated with the work of Alterman *et al.* (1959), who determined the periods of spheroidal oscillations of a spherically symmetric non-rotating Earth. Today, one of the most commonly used, 'battle-tested' (Nolet 2008, p. 163), and openly available programs to compute the free oscillations of a planet is `MINEOS` (Masters *et al.* 2011).

The main challenge in the numerical computation of normal modes stems from the free surface boundary condition as this takes the form of a determinant of a matrix that should vanish. As all entries of this matrix are only known to finite accuracy and the determinant is computed as the difference of large numbers, its computation becomes numerically unstable. This complicates the detection of eigenfrequencies, where the boundary condition is fulfilled. Moreover, the algorithm has to find the complete spectrum of eigenfrequencies below a certain cut-off frequency and these can be arbitrarily close to each other, in particular for spheroidal modes, such that bracketing individual modes is difficult.

The reformulation of the underlying operator into minors and the introduction of mode counters by Woodhouse (1988) largely addressed the aforementioned issues. However, as mode counting is based on detection of the zero crossings of the characteristic function that is only known to finite accuracy, finding all modes in a reliable way remains a challenge, particularly at high frequencies. Additionally, the identification of Stoneley and Slichter modes to high accuracy remains problematic, as the eigenfunctions are vanishingly small at the surface, where the boundary condition needs to be imposed by correct summation of the fundamental solutions.

Possibly the first work to use spectral elements for the calculation of normal modes (in the time domain) is that of Chaljub & Valette (2004). Here, we apply the spectral element method to discretize the weak form of the second-order ordinary differential equations (ODEs) of motion and formulate a generalized matrix eigenvalue problem in the spectral domain. We apply an iterative solver to this problem, whereby we circumvent all aforementioned issues related to the integration methods. In particular, all boundary conditions at the free surface, internal discontinuities, and the centre of the planet are readily implicitly fulfilled in the weak form, such that Stoneley (Stoneley 1924) and Slichter (Slichter 1961) modes pose no particular challenge. Modern Krylov-subspace solvers reliably find all eigenvalues (Hernandez *et al.* 2005), including degenerate eigenvalues, such that finding the complete spectrum is straightforward without the need for a mode counter.

Matrix-based approaches have previously been proposed by Wiggins (1976) and Buland & Gilbert (1984), but both the theory of (higher-order) finite element methods and available numerical software for solving eigenvalue problems have seen a lot progress since. More recently, Zábranová *et al.* (2017) used Chebychev polynomials to discretize the strong form of the equations to derive a matrix formulation of the eigenvalue problem. In their approach, the matrices are non-sparse and non-symmetric and the boundary conditions need to be treated explicitly. A direct eigenvalue problem solver that always computes the full spectrum is used, leading to computation times that are substantially longer than `MINEOS`. In an effort to improve computational efficiency, we derive sparse and symmetric matrices and only solve for the eigenpairs of interest through an iterative solver.

In the following, we briefly describe the underlying theory (detailed treatments can be found in Takeuchi & Saito 1972; Dahlen & Tromp 1998; Woodhouse & Deuss 2015), adhering to the notation of Dahlen & Tromp (1998, Section 2). Following this, we detail the methodology behind the use of spectral elements for the discretization of the weak form of the ODEs and the computation of normal modes in general (Section 3). Next, we apply our method to the computation of toroidal and spheroidal normal mode spectra for several planetary bodies, including Earth, Mars and the Galilean moon Europa, and compare results with those obtained using other numerical schemes (Section 4). Finally, the python-based implementation of the normal mode spectral element method presented herein (spectral element normal mode code; `specnm`) is available open source (see data availability section).

## 2 THEORY

### 2.1 Radial scalar equations

For spherically symmetric, non-rotating, elastic (SNRE) planets, the wave equation can be simplified by a separation of variables in spherical coordinates, for example by using vector spherical harmonics (Dahlen & Tromp 1998) as an Ansatz for the displacement eigenfunctions. This leads to a set of ODEs with the radius of the planet as the only coordinate and where the dependence of the solution on latitudinal and longitudinal coordinates is readily incorporated via spherical harmonics (see Appendix A and Dahlen & Tromp (1998)).

Normal modes are classified in two types as toroidal $T$ (SH or Love wave interference) or spheroidal $S$ ($P$–$SV$ or Rayleigh wave interference) modes. Hereinafter, we denote $n \in [0, \infty)$ as the radial order or overtone number, $l \in [0, \infty)$ as the angular degree and $m$ as the azimuthal order in the range $-l \leq m \leq l$. The asymptotic angular wavenumber that is associated with each mode is defined as $k = \sqrt{l(l+1)}$.

We further denote the toroidal displacement eigenfunctions as $W(r)$ and the spheroidal displacement eigenfunctions as $U(r)$ and $V(r)$. Since spheroidal oscillations also involve changes in density, and therefore perturbations in the gravitational potential, we define the associated function $P(r)$ through an additional coupled ODE. The spheroidal modes with angular degree $l = 0$ are a special case and are called radial modes, as the horizontal displacement vanishes and the system of ODEs is simplified to a single second-order ODE. Toroidal modes only exist for angular degrees $l \geq 1$. The toroidal mode ${}_0\mathrm{T}_1$ and the spheroidal mode ${}_0\mathrm{S}_1$ correspond to solid body rotation and translation, respectively, with a zero eigenfrequency and are thus discarded in the computation of synthetic seismograms. It should be noted here, that for spherically symmetric non-rotating bodies, the azimuthal order $m$ does not appear in the equations and the eigenfrequencies are thus degenerate with multiplicity $2l + 1$. The eigenfrequencies and radial eigenfunctions are then uniquely determined by their angular degree $l$ and overtone number $n$ so that the modes of both types are identified as ${}_n\mathrm{T}_l$ and ${}_n\mathrm{S}_l$.

To achieve symmetry, the weak form is usually derived from the second-order form of the ODE in wave propagation problems. Here, we derive the second-order ODEs for all three mode types and for transversely isotropic media (parametrized by the Love parameters $A$, $C$, $L$, $N$, $F$ and density $\rho$) from the more commonly-used first-order form (Appendix A).

For toroidal oscillations, we obtain a second-order ODE by taking the radial derivative of the toroidal first-order equation (eq. A1) and inserting the expression for the radial derivative of the traction (eq. A2):

$$\rho\omega^2 W = -\partial_r T_W + (k^2 - 2)Nr^{-2}W - 3r^{-1}T_W, \tag{1}$$

where the traction $T_W(r)$ is given by (Dahlen & Tromp 1998, eq. 8.193)

$$T_W = L(\partial_r W - r^{-1}W). \tag{2}$$

The boundary conditions are given in Table 1, which together with the jump condition at the internal discontinuities that follows from the continuity of the eigenfunctions and tractions, define the solution space.

For spheroidal oscillations there are three coupled second-order ODEs corresponding to the eigenfunctions $U(r)$, $V(r)$ and $P(r)$. As for the toroidal case, the equations for the spheroidal case are obtained by taking the radial derivative of the spheroidal first-order equations

**Table 1.** Boundary conditions for the second-order radial equations for the eigenfunctions $U$, $V$, $W$, $P$ and corresponding tractions $T_U$, $T_V$, $T_W$ and $T_P$. Zero radius (centre of planet) boundary conditions are based on Zábranová *et al.* (2017).

| **Toroidal** | $W(r)$ |
|---|---|
| Free surface and solid–fluid boundary | $T_W = 0$ |
| Zero radius | $W = 0$ |
| **Radial** | $U(r)$ |
| Free surface | $T_U = 0$ |
| Zero radius | $U = 0$ |
| **Spheroidal** | $U(r),\ V(r),\ P(r)$ |
| Free surface | $T_U = T_V = T_P = 0$ |
| Solid side of solid–fluid boundary | $T_V = 0$ |
| Zero radius | $\partial_r U = \partial_r V = P = 0, \quad (l = 1)$ |
| | $U = V = P = 0, \quad (l \geq 2)$ |

(eqs A3–A5) and inserting the tractions (eqs A6–A8):

$$\begin{aligned}
\rho\omega^2 U &= -\partial_r T_U - [4\rho g r^{-1} - 4\left(A - N - C^{-1}F^2\right) r^{-2}]U + [k\rho g r^{-1} - 2k\left(A - N - C^{-1}F^2\right) r^{-2}]V - (l+1)\,\rho r^{-1} P\\
&\quad -2\left(1 - C^{-1}F\right) r^{-1} T_U + k r^{-1} T_V + \rho T_P,\\
\rho\omega^2 V &= -\partial_r T_V + [k\rho g r^{-1} - 2k\left(A - N - C^{-1}F^2\right) r^{-2}]U - [2N r^{-2} - k^2\left(A - C^{-1}F^2\right) r^{-2}]V + k\rho r^{-1} P\\
&\quad -kC^{-1}F r^{-1} T_U - 3r^{-1} T_V,\\
0 &= -\partial_r T_P - 4\pi G\,(l+1)\,\rho r^{-1} U + 4\pi G k\rho r^{-1} V\\
&\quad +(l-1)\, r^{-1} T_P.
\end{aligned} \tag{3}$$

Here the tractions $T_U(r)$, $T_V(r)$ and $T_P(r)$ are defined as:

$$\begin{aligned}
T_U &= C\partial_r U + F r^{-1}(2U - kV),\\
T_V &= L(\partial_r V - r^{-1} V + k r^{-1} U),\\
T_P &= \partial_r P + 4\pi G\rho U + (l+1) r^{-1} P,
\end{aligned}$$

where $G$ denotes the gravitational constant and $g(r)$ the gravitational acceleration in the undeformed planet, which is uniquely determined from the density profile $\rho(r)$. The boundary conditions can be found in Table 1 and continuity of eigenfunctions and tractions holds as in the toroidal case.

For short-period oscillations, self-gravity plays a negligible role as a restoring force compared to the elastic forces (Dahlen & Tromp 1998) and the change in the gravitational potential due to the mass redistribution caused by the seismic disturbance can be omitted [for a quantitative error estimate see fig. 1 in van Driel *et al.* (2021a)]. This approximation is known as the Cowling approximation (Cowling 1941; Dahlen & Tromp 1998). In the Cowling approximation, the system of governing equations reduces to two coupled second-order ODEs for $U(r)$ and $V(r)$, since the perturbation in the gravity potential and its related eigenfunction $P(r)$ can be excluded. Consequently, the approximated system of ODEs is given by:

$$\begin{aligned}
\rho\omega^2 U &= -\partial_r T_U - [4\rho g r^{-1} - 4\left(A - N - C^{-1}F^2\right) r^{-2}]U + [k\rho g r^{-1} - 2k\left(A - N - C^{-1}F^2\right) r^{-2}]V\\
&\quad -2\left(1 - C^{-1}F\right) r^{-1} T_U + k r^{-1} T_V,\\
\rho\omega^2 V &= -\partial_r T_V + [k\rho g r^{-1} - 2k\left(A - N - C^{-1}F^2\right) r^{-2}]U - [2N r^{-2} - k^2\left(A - C^{-1}F^2\right) r^{-2}]V\\
&\quad -kC^{-1}F r^{-1} T_U - 3r^{-1} T_V.
\end{aligned} \tag{4}$$

The tractions $T_U(r)$ and $T_V(r)$ are the same as in the case with full gravity, and the same boundary conditions apply.

The ODE for spheroidal modes with zero angular degree $l = 0$ (radial modes) consists of a single second-order equation involving the radial displacement eigenfunction $U(r)$ only and is given by:

$$\rho\omega^2 U = -\partial_r T_U - \left[4\rho g r^{-1} - 4\left(A - N - C^{-1}F^2\right) r^{-2}\right] U - 2\left(1 - C^{-1}F\right) r^{-1} T_U. \tag{5}$$

The traction $T_U(r)$ is identical to the one for spheroidal modes with $V(r)$ set to zero. The boundary conditions are again given in table 1.

To ignore gravity completely, it is sufficient to set all terms related to gravity to zero in the Cowling approximation. This includes terms involving either the gravity constant $G$ or the gravitational acceleration $g(r)$. This is particularly useful as a means of benchmarking with time domain methods that do not incorporate the effects of gravity such as AxiSem (e.g. Nissen-Meyer *et al.* 2014).

### 2.2 Weak form

To enable a spectral element formulation, the set of ODEs together with their respective boundary conditions can be transformed from the strong to the weak form. Alternatively, it is also possible to start from the variational principle and vary the action of the respective mode type as shown in Dahlen & Tromp (1998, section 8.6.4). Interpreting the variation of the eigenfunctions as the test function leads to the weak form. Another possibility is to start from the general three-dimensional (3-D) weak form and use spherical harmonics as Ansatz to derive the radial ODEs as shown by Al-Attar & Tromp (2013). Here, we start from the strong form and illustrate the derivation for the toroidal modes (the weak forms for spheroidal and radial modes can be found in appendix B).

To derive the weak form, we multiply the strong form with a test function $\tilde{W}$ and integrate over the radial domain, $\Omega$, of the planet. An additional geometric integral kernel $r^2$ that stems from the volume element is introduced for consistency with the physical normalization and partial integration is applied to achieve a symmetric form. Note that the weak form is equivalent to the strong form if the equation for the weak form is fulfilled for all test functions from an appropriately chosen set.

Writing this step explicitly for the toroidal eq. (1) gives us:

$$\omega^2 \int_\Omega \rho W \tilde{W} r^2 \,\mathrm{d}r = -\int_\Omega \partial_r T_W \tilde{W} r^2 \,\mathrm{d}r + \int_\Omega N(k^2-2) W \tilde{W} \,\mathrm{d}r - \int_\Omega 3r T_W \tilde{W} \,\mathrm{d}r$$
$$= -\left[T_W \tilde{W} r^2\right]_{r_0}^{r_\mathrm{surf}} + \sum_{r\in d}\left[T_W \tilde{W} r^2\right]_-^+ + \int_\Omega T_W (r^2 \partial_r \tilde{W} + 2r\tilde{W}) \,\mathrm{d}r + \int_\Omega N(k^2-2) W \tilde{W} \,\mathrm{d}r - \int_\Omega 3r T_W \tilde{W} \,\mathrm{d}r. \tag{6}$$

Boundary terms from integration by parts need to be considered for all internal discontinuities $d$, at the free surface $r_\mathrm{surf}$ and at the core-mantle-boundary or at the centre of planets without a liquid core $r_0$. However, these terms vanish at the centre because both $\tilde{W}$ and $r$ are zero here (the same boundary conditions apply to the test function as for the eigenfunctions) and at the free surface or solid fluid boundary, where $T_W$ is zero. At internal discontinuities, the continuity of the eigenfunction $W$ and its related traction $T_W$ ensures that each term appears twice with opposite sign. As a consequence, all boundary conditions are readily implicitly fulfilled. Finally, from the definition of the traction $T_W$ (eq. 2), we arrive at the symmetric weak form:

$$\omega^2 \int_\Omega \rho W \tilde{W} r^2 \,\mathrm{d}r = \int_\Omega L(r\partial_r W - W)(r\partial_r \tilde{W} - \tilde{W}) \,\mathrm{d}r + \int_\Omega N(k^2-2) W \tilde{W} \,\mathrm{d}r. \tag{7}$$

### 2.3 Discretization

Using the Galerkin method, we approximate the solution for the eigenfunction $W(r)$ by a finite set of basis functions $\psi(r)$:

$$W(r) \approx \sum_i w_i \psi_i(r), \tag{8}$$

where $w_i$ are the toroidal expansion coefficients (degrees of freedom). The same basis functions $\psi_i$ are used as test functions in the weak form. Consequently, we end up with the following discrete approximation for the toroidal modes (eq. 7):

$$\omega^2 w_j \int_\Omega \rho \psi_i \psi_j \,\mathrm{d}r = w_j \int_\Omega \left[L(r\partial_r\psi_i - \psi_i)(r\partial_r\psi_j - \psi_j) + N(k^2-2)\psi_i\psi_j\right] \mathrm{d}r, \tag{9}$$

where $w_j$ are again the basis coefficients from the expansion of $W$ as in (eq. 8) and summation over repeated indices is implied. Given the basis function, the integrals can be evaluated and the equation can equivalently be written in matrix form. Identifying the terms for the mass matrix $\mathbf{M}$ and stiffness matrix $\mathbf{K}$ for toroidal modes and denoting $\mathbf{w}$ as a vector containing the coefficients $w_i$, this reads

$$\omega^2 \mathbf{M}\mathbf{w} = \mathbf{K}(l)\mathbf{w}. \tag{10}$$

For the spheroidal case, there is the additional complexity that multiple eigenfunctions need to be included in the eigenvector with a well-defined order. We group the three degrees of freedom for each basis function together, such that in the case of full gravity with eigenfunctions $U(r)$, $V(r)$ and $P(r)$, the vector reads $(u_0, v_0, p_0, u_1, v_1, p_1, \ldots)$, where $u_i$, $v_i$ and $p_i$ are the spheroidal basis coefficients from the expansion of $U$, $V$ and $P$, respectively.

### 2.4 Spectral elements

The spectral element method consists of a particular choice of test functions together with a quadrature rule to approximate the integrals of the weak form. The challenge in finding an appropriate set of test functions is to come up with functions that fulfil the boundary conditions at all internal discontinuities, while guaranteeing higher-order convergence of the method to efficiently achieve a high level of accuracy. The first condition is solved by subdividing the domain into $N_e$ subdomains $\Omega_e$ called elements, such that the internal discontinuities of the model align with element boundaries. To address the second condition, the solution within each element is expanded in terms of $p+1$ Lagrange polynomials $\psi_i^e$ ($i = 1,..., p+1$) of degree $p$ on the Gauss–Lobatto–Legendre (GLL) points. These points represent the optimal choice for Lagrange interpolation with the first and last point located on the element boundary (e.g. Igel 2017, eq. 7.33). This particular choice coincides with the optimal points for Gauss quadrature that integrate polynomials of degree $2p-1$ exactly. At element boundaries, continuity of the

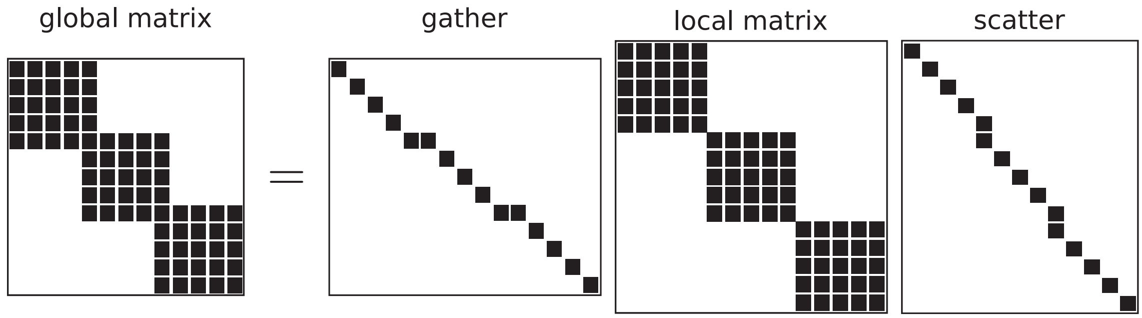


**Figure 1.** Illustration of the local-to-global transformation for DOFs on the boundary of the elements using gather and scatter operators according to (eq. 14). The simplest case is for toroidal modes, where the solution is scalar. For spheroidal modes the solution has multiple DOFs per Gauss–Lobatto–Legendre point, which needs to be reflected in the gather/scatter operators.

test functions is enforced explicitly as discussed in the following and continuity of traction is implied by the weak form as discussed in the previous section.

Given the subdivision of the domain, the integrals over the whole domain in the weak form can be split up into a sum of integrals over all elements. While the integrals could in principal be solved analytically given the test functions, it is common practice to apply a quadrature rule instead. The Gauss quadrature on the GLL points is accurate for polynomials up to degree $2n-1$, while the equations contain terms up to order $2n$. While this implies that the integrals are computed approximately, it is sufficiently accurate to maintain the convergence order of the method (e.g. Cohen & Pernet 2017, p.208). The main benefit of this quadrature is that the mass matrix **M** becomes diagonal as the quadrature points are identical to the interpolation points, that is the Lagrange basis on the GLL point is orthogonal with respect to the GLL quadrature. The mass matrix induces an inner product in the discrete space equivalent to the integrals in the continuous variational principle, such that the discrete weak form of the equation corresponds to a discrete variational principle. If the mass matrix is diagonal this inner product is particularly simple and all integral quantities derived from perturbation theory in the continuous problem (such as attenuation factors, group velocity) hold exactly in the discrete case if the same quadrature is used to approximate the integral.

To evaluate the integral, each element $\Omega_e$ needs to be mapped onto a reference element, which, in the 1-D case considered here, is just the interval $[-1,\ 1]$. This mapping is defined as

$$F_e:\ [-1,1]\to\Omega_e,\qquad r=F_e(\xi),\qquad e\in[1,\ldots,N_e]. \tag{11}$$

We define the Lagrange polynomials of order $p$ within an element by

$$\ell_i^p(\xi):=\prod_{j\neq i}^{p+1}\frac{\xi-\xi_j}{\xi_i-\xi_j}. \tag{12}$$

The element-wise integrals can then be expressed in the reference coordinates $\xi$ and approximated by Gauss quadrature as

$$\int_{\Omega_e} f(r)\,\mathrm{d}r=\int_{-1}^{1} f(\xi)J(\xi)\,\mathrm{d}\xi\approx\sum_{i=1}^{p+1}\sigma_i f(\xi_i)J(\xi). \tag{13}$$

where $J(\xi)$ is the Jacobian given by $J(\xi)=\frac{\mathrm{d}r}{\mathrm{d}\xi}$ and the GLL integration weights are $\sigma_i=\int_{-1}^{1}\ell_i^p(\xi)\,\mathrm{d}\xi$. The derivative of the Lagrange polynomials needed in the discretization of the full equations can readily be derived from the polynomial basis functions.

Requiring continuity of the solution at the element boundaries is simplified by the fact that the GLL points include the boundary. The two DOFs on the boundary of two neighbouring elements correspond to a single global DOF, so no linear system needs to be solved but the mass and stiffness matrices need to be assembled. This can be done in terms of gather and scatter matrices $\mathbf{Q}^{\mathrm{T}}$ and $\mathbf{Q}$ (e.g. Nissen-Meyer *et al.* 2007): The scatter operator copies elements from global-to-local degrees of freedom, while its transpose, the gather operator, sums up element boundary contributions into the single global DOF.

A global operator **A** corresponding to an ODE on the full domain can then be assembled from the element-wise operator $\mathbf{A}_L$ as:

$$\mathbf{A}=\mathbf{Q}^{\mathrm{T}}\mathbf{A}_L\mathbf{Q}. \tag{14}$$

In the 1-D case, where each element has exactly two neighbours and the DOFs can trivially be indexed by sorting along the radius, the gather and scatter operators take a very simple form. The resulting matrix then is a band matrix where the bandwidth is equal to the size of the blocks in the local operator, that is the number of degrees of freedom per element (Fig. 1).

Finally, we can write the ODE in terms of a generalized weakly non-linear matrix eigenvalue problem

$$\omega^2\mathbf{M}\mathbf{s}=\mathbf{K}(l,\omega)\mathbf{s}, \tag{15}$$

where $\mathbf{K}(l,\omega)$ is the positive definite stiffness matrix that is a function of angular degree $l$ and frequency $\omega$. This is the case when attenuation is taken into account, in which case the material parameters become frequency-dependent (see Section 3.4 for details). **M** is the mass

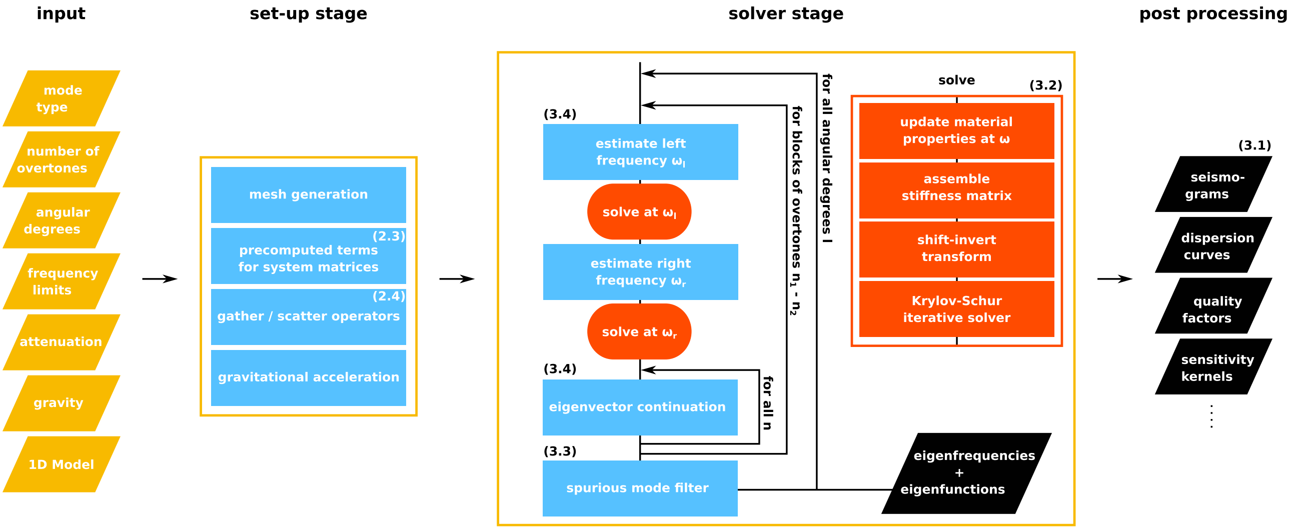


**Figure 2.** Logical flow chart of the `specnm` software as summarized in Section 3.1. Numbers in parenthesis indicate sections where details of the respective step can be found.

matrix, which is positive semi-definite for the spheroidal equation with full gravity and positive-definite otherwise. The system can be solved numerically for the **M**-orthonormalized eigenvectors ${}_n\mathbf{s}_l$, where $n$ is the overtone number and to each of these eigenvectors there exists a corresponding eigenfrequency ${}_n\omega_l$.

## 2.5 Fluid layers

In fluid layers ($L = N = 0$), the shear traction $T_V$ vanishes and the horizontal displacement $V$ can be computed from the other two degrees of freedom (Dahlen & Tromp 1998, eq. 8.143). However, due to the occurrence of $\omega^2$ in this relation, this replacement would render the eigenvalue problem quadratic. Typically, quadratic eigenvalue problems are transformed to linear problems, doubling the size of the matrices in the process. To avoid this complication, we follow the same approach as Wiggins (1976), Buland & Gilbert (1984) and Zábranová *et al.* (2017) and keep the same representation of the solution in the fluid as in the elastic part of the domain. If the boundary condition on the solid side of the solid-fluid boundary is correctly set (no horizontal traction, $T_V = 0$) then the eigenvectors are computed correctly both in the fluid and the solid. This boundary condition again corresponds to the natural boundary condition of the weak form of the equations. As a result, it is easily implemented by dropping the explicit condition of continuity of $V$ at the solid–fluid boundary in the gather and scatter operators. The additional degrees of freedom in the fluid are not constrained by the physics and lead to spurious, that is unphysical, additional solutions of the discrete system (Wiggins 1976). The spurious modes, how they differ from the undertones discussed by Buland & Gilbert (1984) and our filtering technique to remove them from the spectrum will be further discussed in Section 3.3.

# 3 NUMERICAL IMPLEMENTATION

## 3.1 Overview of the workflow

The schematic workflow for computing complete catalogues of normal modes as implemented in our software *specnm* is shown in Fig. 2. In the following, we provide an overview after which we detail the most important steps. The workflow is divided into three main parts:

First, a `set-up stage` generates the mesh based on the `input` 1-D model and frequency range, such that each discontinuity in the model aligns with an element boundary and the element size is smaller than a given fraction of the *S*-wavelength (*P*-wavelength in the fluid). In the examples shown below, we find that two elements per wavelength with a polynomial order $p = 5$ provides sufficient accuracy. The model parameters are subsequently converted to the transverse isotropic parameters ($A$, $C$, $L$, $N$, $F$, see e.g. Dziewonski & Anderson 1981), the most general elastic medium with spherical symmetry, and the gravitational acceleration as a function of the radius $g(r)$ is computed from the density profile by numerical integration. Given the discretization and model parameters, the gather and scatter operators, mass matrix, and all terms needed to build the stiffness matrices can be precomputed. As the stiffness matrix is a function of the angular degree and frequency through the material parameters, it is split into terms independent of the angular degree $l$ and the material properties (see eq. 15). Assembly of the full stiffness matrix is then efficiently implemented as a series of sparse matrix operations.

Secondly, a `solver stage` computes the normal mode catalogue by iterating over all angular degrees $l$ and computing all overtones $n$ up to a user-defined frequency $f_{\max}$. If the frequency dependence of the material parameters due to attenuation is ignored, the eigenvalue problem is linear and the eigenpairs can be directly computed (see Section 3.2). If this is not the case, the stiffness matrix needs to be updated as a function of frequency and we solve the non-linear problem using eigenvector continuation in an inner loop over overtones (see Section 3.4). In the spheroidal case with fluid layers, the spurious modes need to be filtered from the mode spectrum (Section 3.3).

Thirdly, once the eigenfrequencies and eigenfunctions are known, the decay factors $\gamma = \frac{\omega}{2Q}$ (from first order perturbation theory), dispersion curves, sensitivities as well as the displacement $\mathbf{s}(\mathbf{x}, \omega)$ at any location within the planet can be calculated by summation over all angular degrees $l$ and overtones $n$ (Dahlen & Tromp 1998, eq. 10.61) in a `post processing` stage:

$$\mathbf{s}(\mathbf{x}, t) = \sum_{n=0}^{\infty} \sum_{l=0}^{\infty} {}_n\mathbf{A}_l(\mathbf{x}) {}_n\omega_l^{-2} [1 - \cos({}_n\omega_l t) \exp(-{}_n\gamma_l t)]. \tag{16}$$

Here, the amplitude factor ${}_n\mathbf{A}_l$ is computed from the eigenfunctions and a given source location, depth and moment tensor. For comparison to `MINEOS`, the corrections of the eigenfunctions for the response of a seismometer on Earth's surface need to be included (Dahlen & Tromp 1998, eq. 10.71–72).

### 3.2 Numerical solution of the eigenvalue problem

While small eigenvalue problems can be solved directly via matrix decomposition, it is more efficient to use iterative methods, such as the Lanczos or Arnoldi methods, for large matrices (Lehoucq *et al.* 1998). This is particularly true for sparse matrices and in case that only a fraction of the eigenvalue spectrum needs to be computed. For the particular matrices in the problem we consider here, we found a modern variation of the Arnoldi method called implicitly restarted Krylov–Schur (Hernandez *et al.* 2005) to be efficient and reliable.

Iterative eigenvalue solvers converge to eigenvalues successively, starting from the largest. In the normal mode problem, we are interested in small eigenvalues, but not necessarily the smallest because of the presence of undertones (Buland & Gilbert 1984). The undertones for a fixed angular degree $l$ have eigenfrequencies that accumulate at zero with an infinite number of modes below any finite frequency. To select the range of eigenvalues of interest, we apply a shift-invert method and solve the corresponding auxiliary problem in which the eigenvalues of interest are in fact the largest (Scott 1982). Importantly, this method can be applied to the generalized eigenvalue problem with a semi-definite mass matrix, as in the case of spheroidal modes with full gravity.

The auxiliary problem of the shift-invert method is defined as

$$(\mathbf{K} - \sigma\mathbf{M})^{-1}\mathbf{M}\mathbf{s} = \mathbf{C}\mathbf{s} = \mu\mathbf{s}, \tag{17}$$

where $\sigma$ is the shift-value around which the eigenvalues are sought, $\mu$ is the eigenvalue of the auxiliary problem and related to the eigenvalue $\omega^2$ of the original problem by

$$\mu = \frac{1}{\omega^2 - \sigma}. \tag{18}$$

The eigenvectors remain identical under this transformation.

As $\mathbf{K}$ is banded (see Fig. 1) and $\mathbf{M}$ is diagonal, the inverse can be computed via sparse LU decomposition (Amestoy *et al.* 2001) and the fill-in is limited to the bandwidth of $\mathbf{K}$. The iterative solution for the eigenvalues hence remains highly efficient under this transformation.

The convergence criterion to accept the eigenvalues from the iterative method is based on the $L_2$-norm of the residuum vector of the generalized eigenvalue problem

$$\mathbf{r} = (\mathbf{K} - \omega^2\mathbf{M})\mathbf{s} \tag{19}$$

scaled by the matrix norms of the mass and stiffness matrices:

$$\epsilon > \|\mathbf{r}\|_2 / \left(\|\mathbf{K}\|_2 + \omega^2\|\mathbf{M}\|_2\right). \tag{20}$$

This scaling is crucial as the matrix norms can vary significantly and this choice guarantees consistently small relative errors on the eigenvalues. By default, we conservatively choose $\epsilon = 10^{-12}$, as potential performance gains for larger residuals appear marginal in the cases we consider below. Importantly, this criterion only refers to the discrete problem. An estimation of the error of the eigenvalue for the continuous problem is discussed in the next section.

### 3.3 Spurious modes and undertone filter

Spurious modes have previously been reported in matrix-based approaches in the spheroidal case for planets with fluid layers (Wiggins 1976; Buland & Gilbert 1984; Zábranová *et al.* 2017). While Wiggins (1976) attributed their presence to the overparametrization in the fluid, where only two of the three eigenfunctions are linearly independent, Buland & Gilbert (1984) attributed them to under-resolved undertones that can be mapped to higher frequency in the discrete system. Here we will argue that both interpretations are partially valid and that two corresponding distinct additional mode types can be identified.

Undertones occur in fluid layers that are not neutrally stratified, as a consequence of which the Brunt–Väisälä frequency is non-zero (Dahlen & Tromp 1998, section 8.8.11). The dominant forcing for these modes is gravitational and derives from density and buoyancy changes as the material experiences a difference in pressure when displaced vertically. In contrast to modes dominated by elastic forces,

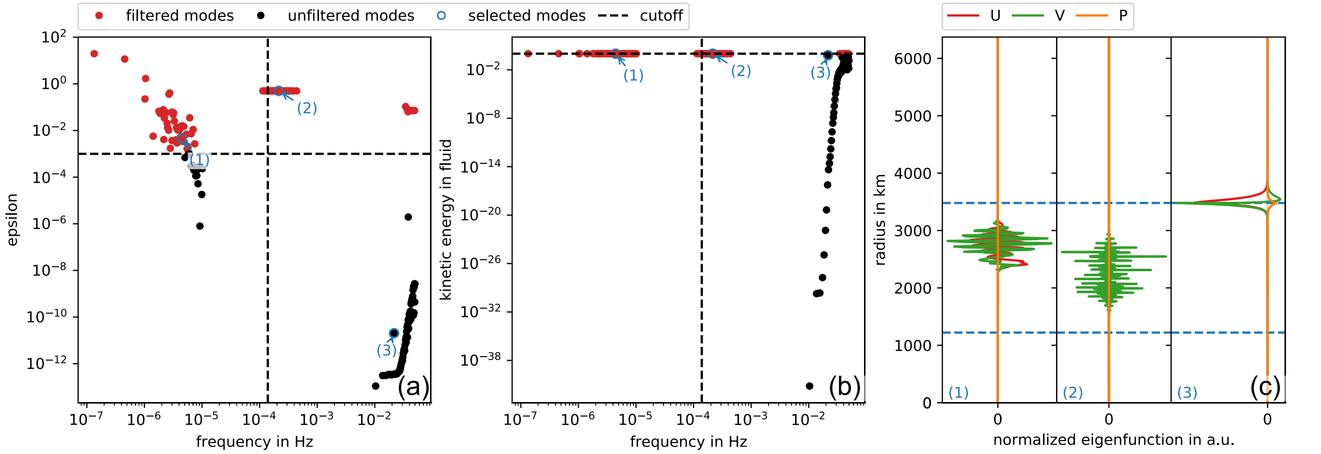


**Figure 3.** Detection of three classes of modes for anisotropic PREM and spheroidal modes with full gravity. In both (a) and (b), the horizontal dashed lines indicate the cut-off rayleigh quotient epsilon and cut-off kinetic energy in fluid, while the vertical dashed lines show the frequency cut-off used for the filtering of the modes. (a) The Rayleigh quotient filter identifies well-resolved solutions, corresponding to the physical modes of interest and long-wavelength undertones. (b) The normalized fluid kinetic energy is used to separate the modes of interest from undertones and spurious modes. (c) Eigenfunctions of three modes representative of the different classes are labelled (1), (2), and (3) in panels (a) and (b).

these modes have very low eigenfrequencies despite having highly complex eigenfunctions. The maximum frequency of the undertones is bound by the maximum of the Brunt–Väisälä frequency as a function of depth. As a consequence, the undertones violate the typical meshing criterion based on the seismic velocities and may have arbitrarily high errors relative to the corresponding solution of the continuous equation. Importantly, we do not observe this class of solutions in the discrete system when the Cowling approximation is used and $P = 0$, although undertones may in principle still exist. In any case, we do not observe a mapping of the discrete eigenfrequencies of the undertones into the elastic eigenfrequency range, in contrast to earlier suggestions by Buland & Gilbert (1984).

A second class of spurious modes can be observed independently of gravity and as there is no correspondence in the continuous solution, the Rayleigh quotient error $\epsilon$ (Takeuchi & Saito 1972) is consistently high. These modes overlap with the elastic modes of interest in the spectrum and we identify the modes through the interpretation of Wiggins (1976).

Buland & Gilbert (1984) use the fraction of kinetic energy in the fluid as a discriminant for these additional modes $E_{\mathrm{kin}}(\Omega_{\mathrm{fluid}})/E_{\mathrm{kin}}(\Omega)$, where the kinetic energy is given by (Dahlen & Tromp 1998)

$$E_{\mathrm{kin}}(\Omega) = \int_{\Omega} \rho(U^2 + V^2) r^2 \, \mathrm{d}r. \tag{21}$$

While this seems appropriate for almost all modes, we nevertheless find that some of the modes belonging to the second class may also include non-zero energy in the elastic part, rendering this criterion by itself unreliable. Instead, we use a combined criterion of Rayleigh quotient error $\epsilon_{\mathrm{RQ}}$ and fluid kinetic energy together with a minimum frequency [for an early discussion on this see Valette (1987)] to separate the three mode types. Thus, if any mode in the frequency range of interest has a high Rayleigh quotient error but a low fluid kinetic energy, the separation fails and mesh refinement or a higher order polynomial is required to ensure that this mode is either well-resolved or correctly identified as spurious.

Importantly, the discrete Rayleigh quotient is exactly what the eigenvalue solver minimizes, so we cannot compute it directly using the mass and stiffness matrices in the same discretization. Instead, we interpolate the eigenfunctions to the next higher polynomial degree and use GLL quadrature to approximate the integrals in the analytical expressions of the Rayleigh quotient for the anisotropic case (Dahlen & Tromp 1998, eqs 8.126–130, 8.208). This ensures exactness of quadrature and provides a reliable and efficient estimator for the relative error of the eigenfrequency of the continuous problem as suggested by Takeuchi & Saito (1972), which is given by

$$\epsilon_{\mathrm{RQ}} = \frac{1}{2}\left(\frac{E_{\mathrm{pot}}}{\omega^2 E_{\mathrm{kin}}} - 1\right), \tag{22}$$

where $E_{\mathrm{pot}}$ is the total potential energy and the additional factor $\frac{1}{2}$ is needed to propagate the error from the eigenvalue to the eigenfrequency.

Fig. 3 shows a comparison of the three mode types and their Rayleigh quotient error $\epsilon_{\mathrm{RQ}}$ as well as their fluid energy. While the Stoneley mode has a high fluid kinetic energy, it is non-zero also in the elastic part and has a low Rayleigh quotient error. Both the spurious modes and the undertones are concentrated in the fluid and have a high Rayleigh quotient error. The spurious mode, however, has oscillations at the resolution limit, while the physical undertone is significantly smoother.

### 3.4 Attenuation

As a consequence of the Kramers–Kronig relations and causality, attenuation of the elastic waves is directly related to the frequency dependence of the elastic moduli, that is, physical dispersion. This results in a weakly frequency-dependent stiffness matrix and consequently

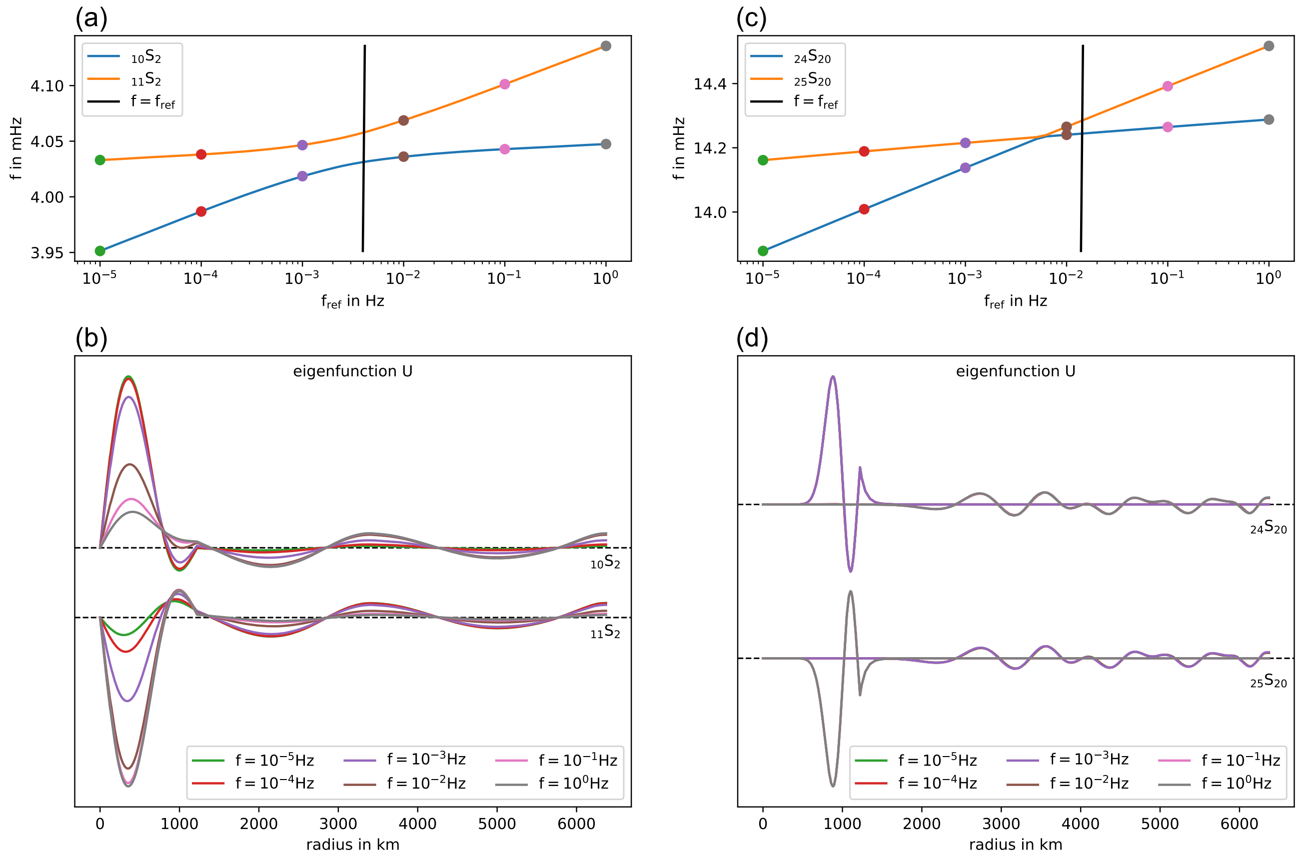


**Figure 4.** Illustration of avoided [subfigures (a) and (b)] and true mode crossings [subfigures (c) and (d)]. (a) Avoided crossing of $_{10}S_2$ with $_{11}S_2$ and (c) true crossing of $_{24}S_{20}$ with $_{25}S_{20}$ as a function of the reference frequency at which the material properties are evaluated. In the vicinity of an avoided crossing, the radial eigenfunctions $U$ of these spheroidal modes exchange character (b), rendering the perturbation of the eigenfrequencies non-linear. This is not the case for a true crossing (d).

a weakly non-linear eigenvalue problem. Instead of using perturbation theory to only correct the eigenfrequencies and not the eigenfunctions for the frequency-dependence, we follow the same approach as established in `MINEOS` and other codes and include the physical dispersion by evaluating the model parameters at the frequency of the mode. The amplitude decay due to attenuation (i.e., the imaginary part of the eigenfrequency) is thus incorporated in the computation of the seismograms. Although exact methods are available (Tromp & Dahlen 1990), this approximation has proven accurate enough for most applications (e.g. Dahlen & Tromp 1998; Al-Attar 2007, and references therein).

Assuming the quality factors $Q$ to be independent of frequency $\omega$ and that the five elastic parameters $\alpha \in \{C, F, N, L, A\}$ are specified at a given frequency $\omega_0$ in the 1-D model of interest, the elastic parameters can be evaluated at any frequency $\omega$ using the logarithmic relation (Dahlen & Tromp 1998)

$$\alpha(r, \omega) \propto \alpha(r, \omega_0) \ln\left(\frac{\omega}{\omega_0}\right). \tag{23}$$

As solvers for non-linear eigenvalue problems are much less developed than for linear problems and the solutions of the normal mode problem are only weakly non-linear, we adopt a strategy based on linear solvers. This is as an extension of the approach by Zábranová *et al.* (2017), who proposed to solve the full eigenvalue problem at a series of fiducial frequencies and then used interpolation to obtain the eigenfrequencies, eigenfunctions and attenuation factors of the non-linear problem. As mentioned by Zábranová *et al.* (2017), one problem that arises is the association of the modes between the eigenvalues computed at different reference frequencies for spheroidal modes, related to the observation that some eigenfunctions exhibited a strong dependence on the reference frequency.

We confirm this observation and provide an interpretation in Fig. 4. As eigenvalue branches may cross as a function of reference frequency, there are two distinct types of crossings: avoided and true crossings. Avoided crossings or level repulsions are well known for overtone branches as a function of angular degree (Dahlen & Tromp 1998) and have been observed in several studies of normal mode coupling (Park 1986; Snieder & Sens-Schönfelder 2021). In the particular case illustrated in Fig. 4, we observe that the eigenvalues of $_{10}S_2$ and $_{11}S_2$ avoid a crossing close to their eigenfrequencies in PREM. The eigenfunctions overlap and exchange character in the avoided crossing, that is, the eigenfunctions of the two modes are rotated in a two-dimensional subspace. In contrast, the eigenfunctions of $_{24}S_{20}$ and $_{25}S_{20}$ do not overlap and the eigenvalue branches cross without any interaction. The eigenfunctions switch character from one overtone to the other and the

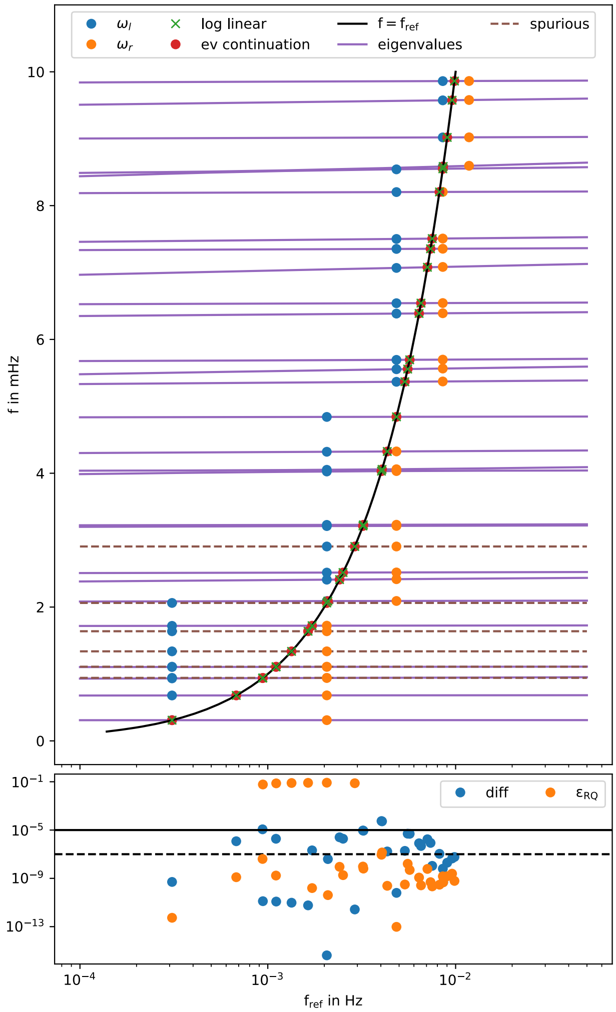


**Figure 5.** Iterative strategy to find the solutions of the non-linear eigenvalue problem for spheroidal modes at angular degree $l = 2$. Firstly, two fiducial frequencies $\omega_l$ and $\omega_r$ are used to bracket blocks of eigenfrequencies that are shown here in blue and orange. Secondly, log-linear interpolation is applied to update the stiffness matrix that results in the solutions depicted by the green crosses. Lastly, eigenvector continuation improves the accuracy of eigenpairs giving the solution for the modes depicted by the red circles. This solution has a much higher accuracy than the simple solution we get by applying the log-linear interpolation as shown in the bottom panel, which indicates the relative difference between the log-linear interpolation and the final solution in blue and the estimate of the final relative error $\epsilon_{\rm RQ}$ of the eigenvalue based on the Rayleigh quotient.

eigenvalues are log-linear in the reference frequency. In order to achieve a reliable association of branches across discretely sampled reference frequencies as required for interpolation of the eigenfrequencies, a dense sampling is required.

Using the iterative solver with the shift-invert method as described in Section 3.2 is most efficient if a small number (between 5 and 20) of eigenvalues are computed at once for a fixed reference frequency due to the overhead related to updating the stiffness matrix and computing the inverse for the auxiliary problem. We thus follow the approach illustrated in Fig. 5: we first solve the linear problem for a block of eigenfrequencies which is bounded by two fiducial reference frequencies. Importantly, the difference between the two reference frequencies is small, as a result of which the eigenfunctions only change slightly and the aforementioned association problem does not occur. In the next step, we estimate the eigenfrequency of the mode by log-linear interpolation between the fiducial frequencies. As the interpolation has no closed-form solution, we use numerical root-finding instead of the *ad hoc* relation proposed by Zábranová *et al.* (2017, eq. 68). Using the resulting approximate eigenfrequency, we update the stiffness matrix and use the eigenfunctions computed at the two fiducial frequencies as a basis in a Rayleigh–Ritz approach (Dahlen & Tromp 1998) to account for the potential non-linearity close to avoided crossings. This idea is also called 'eigenvector continuation' in other fields (e.g. Frame *et al.* 2018) and we summarize the main steps in the following.

First, the mass and stiffness matrix are projected into the subspace spanned by the two eigenfunctions $\mathbf{s}_l$, $\mathbf{s}_r$ computed at the fiducial reference frequencies $\omega_l$, $\omega_r$:

$$\mathbf{N} = \begin{pmatrix} \mathbf{s}_l^T \mathbf{M} \mathbf{s}_l & \mathbf{s}_r^T \mathbf{M} \mathbf{s}_l \\ \mathbf{s}_l^T \mathbf{M} \mathbf{s}_r & \mathbf{s}_r^T \mathbf{M} \mathbf{s}_r \end{pmatrix} \tag{24}$$

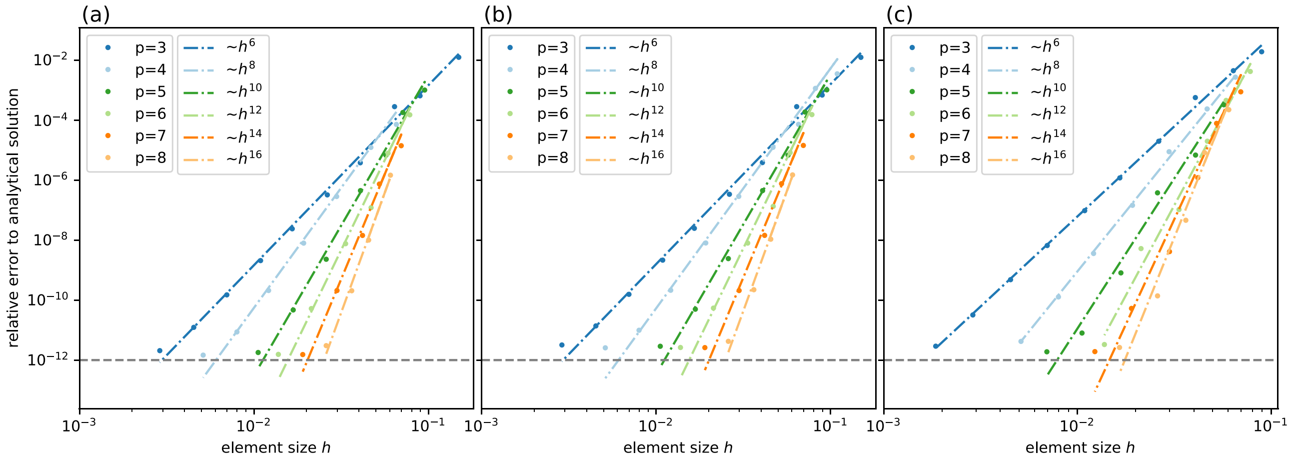


**Figure 6.** Relative error of eigenvalues compared to the analytical solution for the homogeneous sphere for spheroidal modes with (a) full gravity, (b) without gravity and (c) for toroidal modes. The error is calculated for angular degree $l = 5$, and we show the mean relative error of the first 10 overtones $n < 10$ as a function of the element size $h$. As expected based on theoretical consideration, the eigenvalues converge with order $h^{2p}$.

$$\mathbf{H} = \begin{pmatrix} \mathbf{s}_l^T \mathbf{K} \mathbf{s}_l & \mathbf{s}_r^T \mathbf{K} \mathbf{s}_l \\ \mathbf{s}_l^T \mathbf{K} \mathbf{s}_r & \mathbf{s}_r^T \mathbf{K} \mathbf{s}_r \end{pmatrix}, \tag{25}$$

The solution of the 2-D generalized eigenvalue problem

$$\omega^2 \mathbf{N} \mathbf{v} = \mathbf{H} \mathbf{v} \tag{26}$$

then provides the eigenvalue $\omega^2$ and basis coefficients as eigenvector $\mathbf{v}$ to reconstruct the eigenfunction in the original solution space of the spectral elements.

As this method only requires a few sparse matrix–vector products and the solution of a 2-D eigenvalue problem, it is computationally cheap. Yet, it improves the accuracy relative to the log-linear interpolation by approximately two orders of magnitude (*cf.* lower panel in Fig. 5). Note that although the spurious modes are well-behaved throughout this process, we include them in the figure here for the purpose of illustration, but always filter them out in a final step.

### 3.5 Accuracy of the method

One major advantage of the spectral element method is the flexibility in choosing the polynomial degree of the Lagrange basis functions. Higher orders typically result in higher efficiency, particularly if high accuracy of the solution is required. Here, we demonstrate that the theoretically expected convergence rates can also be observed in the numerical solution in comparison to analytical solutions on a homogeneous sphere (Takeuchi & Saito 1972; Dahlen & Tromp 1998).

According to Babuška & Osborn (1991), the absolute error in the eigenvalue $\lambda_h$ calculated on a mesh with element size $h$ is bounded by

$$C_1 \|\mathbf{r}\|_2^2 \leq |\lambda_h - \lambda| \leq C_2 \|\mathbf{r}\|_2^2, \tag{27}$$

where $C_1$ and $C_2$ are constants and $\mathbf{r}$ is the residuum of the eigenfunction . $\|\mathbf{r}\|_2$, however, is proportional to $h^p$, where $p$ is the polynomial degree of the test function (Cohen & Pernet 2017). As a consequence, the eigenvalues $\lambda_h$ converge with $\mathcal{O}(h^{2p})$ and the same order is expected for the eigenfrequencies $\omega_h = \sqrt{\lambda_h}$, with the relative error offset by a constant factor (0.5). This result is numerically confirmed for spheroidal modes with full gravity, spheroidal modes without gravity and toroidal modes for a homogeneous elastic sphere in Fig. 6.

## 4 BENCHMARK AND APPLICATIONS

In the following, we benchmark `specnm` against mode catalogues and seismograms calculated for Earth (PREM Dziewonski & Anderson 1981) using `MINEOS` (Woodhouse 1988; Masters *et al.* 2011). To further demonstrate the versatility of `specnm`, we apply the method to models of Mars and Jupiter's moon Europa, two planetary objects that differ in structure from the Earth: the former has a purely liquid core (Stähler *et al.* 2021), whereas the latter consists of a global ice layer that overlies a liquid ocean (Stähler et al. 2018), giving rise to a plethora of interesting seismic phases.

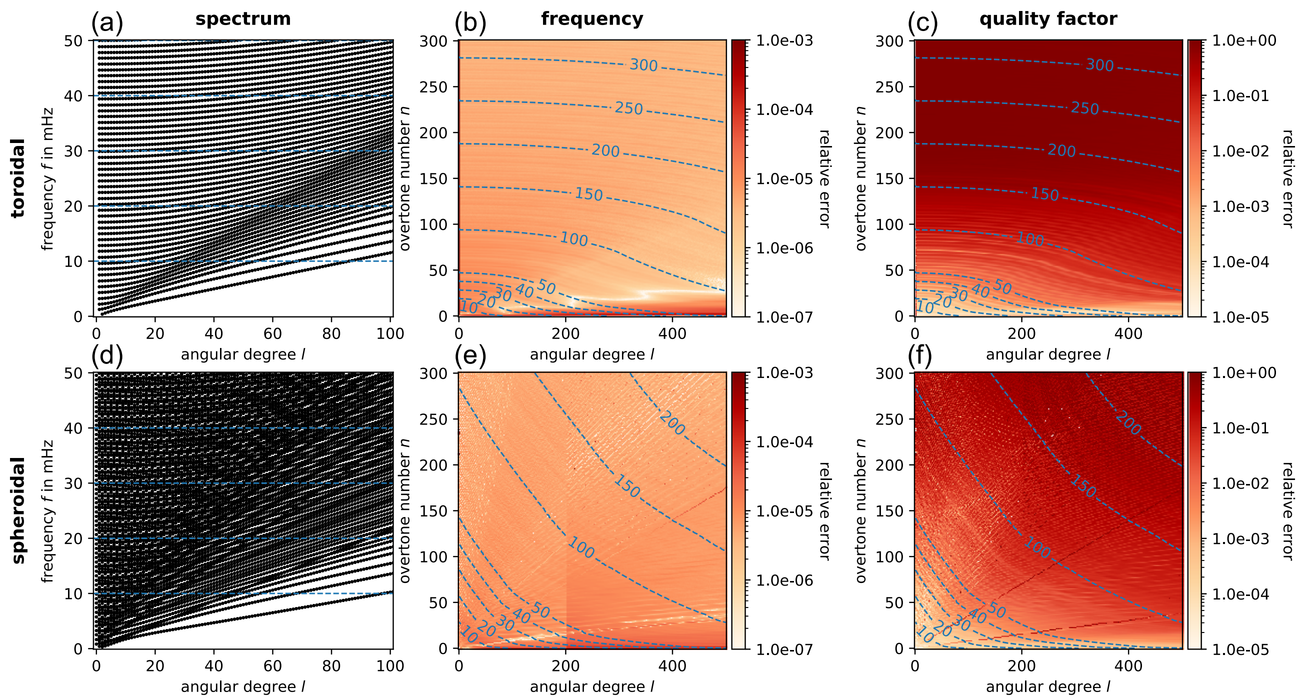


**Figure 7.** Dispersion diagram and comparison of eigenfrequencies and quality factors for toroidal (a–c) and spheroidal (d–f) modes with full gravity computed with `specnm` and `MINEOS`. For the spheroidal case, the Cowling approximation was used in both codes for $l > 200$ due to stability issues with `MINEOS`. Since we were unable to produce the complete spectrum needed for this comparison with `MINEOS`, we had to bi-linearly interpolate the relative error for a small number of modes (13) in the spectrum. Due to the use of the approximation, the subfigures (e) and (f) show a visible discontinuity at angular degree $l = 200$. The dashed light blue curves indicate isofrequency levels in which the labels are given in mHz.

## 4.1 Earth

### *4.1.1 Mode comparison*

Fig. 7 shows a comparison between the results obtained with `specnm` and `MINEOS` in terms of the eigenfrequencies and quality factors $Q$ for both toroidal and spheroidal modes up to a maximum angular degree $l = 500$ and overtone number $n = 300$, corresponding approximately to eigenfrequencies up to 320 and 230 mHz, respectively.

For the majority of the modes, the relative difference of the eigenfrequencies is below $10^{-4}$. Somewhat surprisingly, the relative error is largest for the lowest modes, where the spatial resolution of the spectral element mesh is the highest relative to the complexity of the eigenfunctions. This is most clearly observed for toroidal modes, but is also the case for spheroidal modes. A similar pattern was also observed by Zábranová *et al.* (2017) in the comparison of their method to `MINEOS`, and therefore this is unlikely an issue with `specnm`.

The relative difference of the quality factors is approximately below 1 per cent for most modes with eigenfrequencies smaller than 50 mHz, but becomes unacceptably large at higher frequencies, in particular for Stoneley modes at the core–mantle boundary and the outer-inner core boundary. Again, this was also observed by Zábranová *et al.* (2017). Stoneley modes are known to be particularly challenging for integration methods because of the explicit boundary condition on the free surface, where the eigenfunctions are very close to zero (Dahlen & Tromp 1998). For a verification of our calculation of the attenuation factors independent of other software, we use the linear approximation of the dispersion correction (Dahlen & Tromp 1998, eq. 9.55) and find very good agreement with the non-linear solution if the reference frequency is chosen close to the mode of interest, that is, where the linearization is a good approximation (not shown).

An alternative error quantification for the eigenfrequencies is provided by the Rayleigh quotient error $\epsilon_{\mathrm{RQ}}$ and shown in Fig. 8. Using a polynomial order $p = 5$ and a mesh resolution of two elements per wavelength at the highest frequency, we reliably achieve an error $\epsilon_{\mathrm{RQ}} < 10^{-5}$, which we consider acceptable for most applications. As previously observed by Zábranová *et al.* (2017), the error is largest for the inner-core Stoneley modes, but is more than two orders of magnitude smaller in our work. If higher accuracy is needed for these modes, a mesh refinement around the solid-fluid boundary would be a simple and efficient solution.

In summary, we consider the comparison to `MINEOS` together with the low Rayleigh quotient error and the convergence test in the previous section as a confirmation of the correctness of our implementation.

### *4.1.2 Seismogram comparison*

Fig. 9 shows a comparison between seismograms computed with `specnm` and `MINEOS`. We computed all modes up to a maximum frequency of 40 mHz as eigenfrequencies and attenuation factors computed with `specnm` and `MINEOS` agree reasonably well in this range, and `MINEOS`

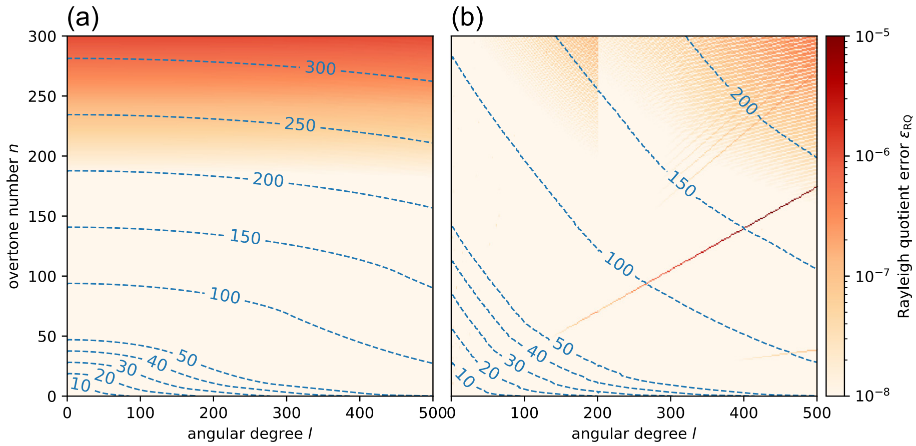


**Figure 8.** Estimate of the eigenfrequency error from the Rayleigh quotient $\epsilon_{\mathrm{RQ}}$ for (a) toroidal and (b) spheroidal modes in PREM. The calculations were performed with polynomial order 5 and a mesh with two elements per wavelength at the maximum frequency. Due to the use of the Cowling approximation for angular degree of $l > 200$, the subfigure (b) shows a visible discontinuity in the Rayleigh quotient $\epsilon_{\mathrm{RQ}}$ at angular degree $l = 200$. The dashed light blue curves indicate isofrequency levels in which the labels are given in mHz.

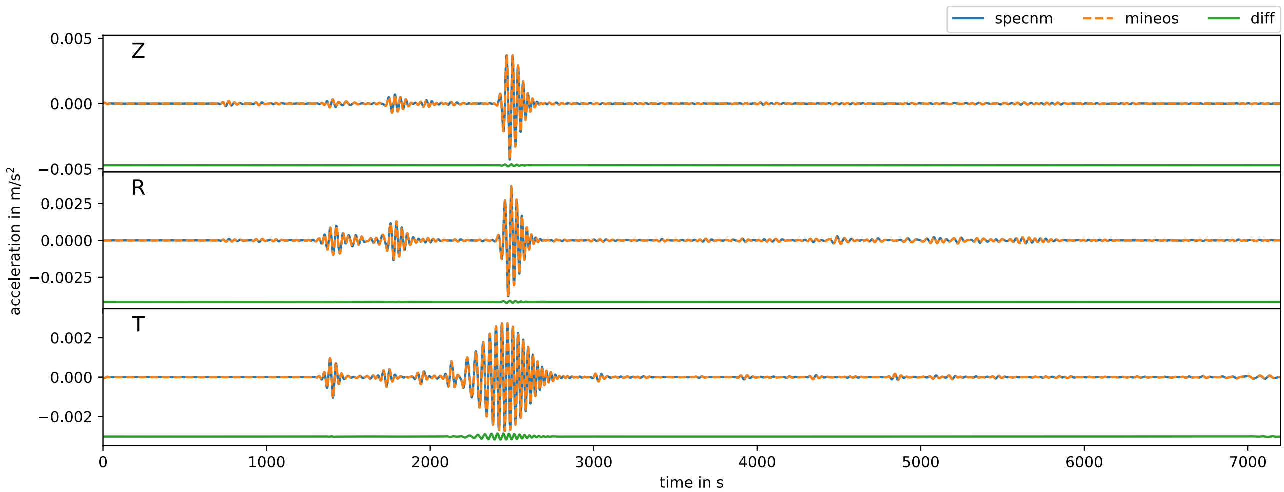


**Figure 9.** Synthetic acceleration seismograms computed for the Tohoku Oki earthquake at the Black Forrest Observatory (BFO) seismic station. Z, R and T refer to vertical, radial and transverse component, respectively. The green line indicates the difference between `MINEOS` and `specnm`. All modes up to 40 mHz are included in both `MINEOS` and `specnm`. A low-pass filter was applied at 33.3 mHz.

reliably computes all modes with full gravity (which is not the case for higher frequencies). For the computation, we use the centroid solution of the 2011 Tohoku Oki earthquake as source and the black forest observatory (BFO) as representative station. Free air, potential and tilt corrections to the eigenfunctions are applied before calculating the excitation coefficients for each mode.

The resultant three-component acceleration seismogram for a duration of 2 hr (after the event) is shown in Fig. 9. The seismograms are low-pass filtered at 33.3 mHz to avoid ringing at the cut-off frequency of the mode catalogues. The difference between `specnm` and `MINEOS` is only a few percent in amplitude relative to the signal, with the largest discrepancy caused by slight phase shifts of the fundamental mode surface waves, as expected from the difference in eigenfrequencies discussed above. We also computed and compared spectra from the seismograms, which are illustrated in Fig. 10. The spectra are computed over a time window of 24 hr. The spectra are seen to be commensurate, with the largest difference again occurring on the transverse component, which is dominated by toroidal modes. This provides further evidence for the proper calculation of long-period seismograms.

### 4.2 Mars

Normal mode seismology on Mars has been considered in the context of theoretical and pre-mission (e.g. Viking 1 and 2, Mars 96, InSight) science studies on Mars (e.g. Bolt & Derr 1969; Okal & Anderson 1978; Gudkova *et al.* 1993; Lognonné *et al.* 1996; Zheng *et al.* 2015; Bissig *et al.* 2018). Presently, Mars' internal structure is informed by recent observations of seismic body wave phases from marsquakes recorded by the InSight lander (Banerdt *et al.* 2020). The data indicate that Mars consists of a volatile-rich liquid Fe core, an iron-enriched silicate mantle (relative to Earth), and a crust with a thickness in the range 25–45 km (Knapmeyer-Endrun *et al.* 2021; Khan *et al.* 2021; Stähler *et al.*

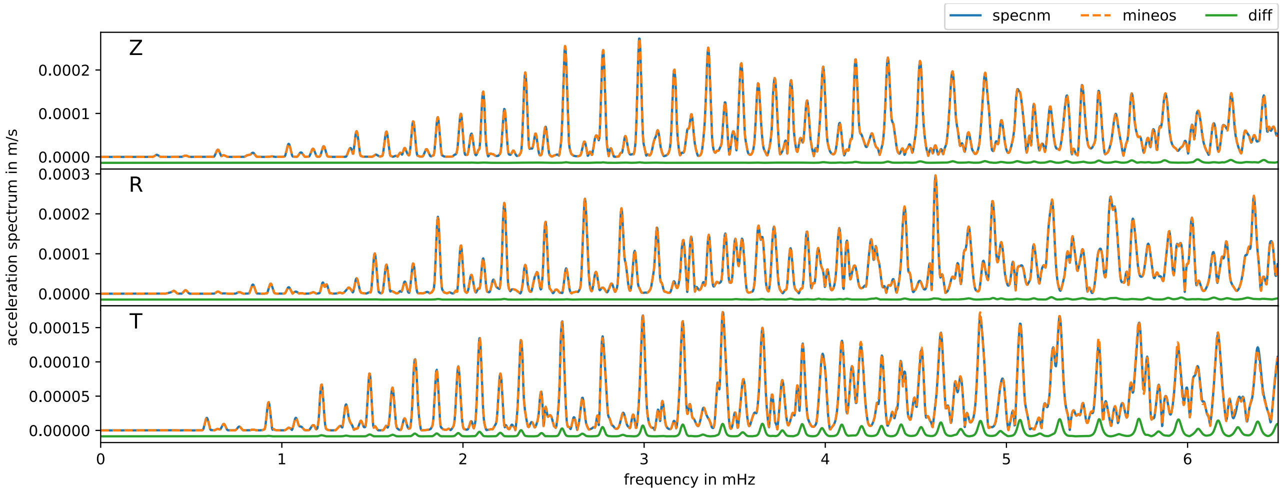


**Figure 10.** Three-component amplitude spectra of the seismic traces shown in Fig. 9 computed from a 24-hr time window. Z, R and T refer to vertical, radial and transverse component, respectively. The difference (green line) is computed as the absolute value of the difference of the complex spectra and therefore mostly shows phase shifts due to the slight difference in the eigenfrequencies of the fundamental mode and first overtones.

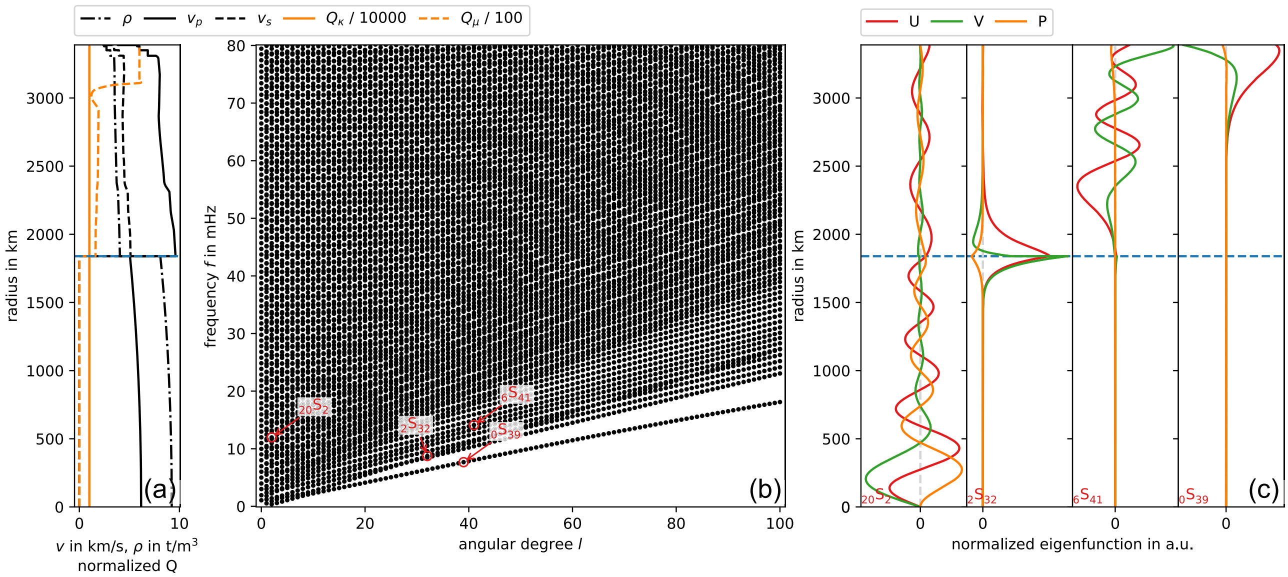


**Figure 11.** Normal mode seismology on Mars. (a) Radially symmetric Mars model. (b) Spheroidal spectrum of modes for Mars using full gravity with fluid core and attenuation. (c) Spheroidal mode eigenfunctions for the modes indicated in (b): ${}_{20}S_2$, ${}_{2}S_{32}$, ${}_{6}S_{41}$ and ${}_{0}S_{39}$. See main text for details.

2021). In anticipation of the detection of normal modes on Mars by InSight, we consider the elastic model shown in Fig. 11(a) from (Stähler *et al.* 2021), augmented with anelastic information from (Khan *et al.* 2018).

The spheroidal mode spectrum with full gravity is shown in Fig. 11(b) and because of the absence of an inner core and associated inner-core-boundary modes appears less complex relative to Earth's spectrum (Fig. 7d). However, as the boundary conditions are all implicitly included in the weak form, this poses no additional challenge to `specnm`. For the four modes marked with red circles in Fig. 11(b), we show the corresponding eigenfunctions in Fig. 11(c): ${}_{20}S_2$ is representative of a core-sensitive mode; ${}_{2}S_{32}$ is a core-mantle boundary (CMB)-sensitive Stoneley mode; ${}_{6}S_{41}$ is exemplary of a mode that has sensitivity throughout the entire mantle; and ${}_{0}S_{39}$ is depictive of an upper mantle-sensitive fundamental mode. Finally, we have tabulated the periods of the first ten fundamental spheroidal and toroidal modes, including their group and phase velocities, for the Mars model considered here in Table 2.

## 4.3 Europa

Europa is the smallest of the four Galilean moons of Jupiter and of intense interest because of its astrobiological potential (Vance *et al.* 2018). Direct, spectroscopic, gravity (Anderson *et al.* 1998) and magnetic field measurements (Khurana *et al.* 1998) suggest that Europa is covered by a global layer of ice lying over an ocean of liquid water. There is evidence, based on an approximate surface age of 10 Myr (Zahnle *et al.* 1998), that geothermal sources and tidal heating is keeping the ocean from freezing. For the calculations performed here, we rely on a

**Table 2.** Selected fundamental mode periods, phase velocities and group velocities for toroidal and spheroidal modes with full gravity for the Mars model shown in Fig. 11.

| Mode | Period in s | Phase velocity (km s$^{-1}$) | Group velocity (km s$^{-1}$) |
|---|---|---|---|
| $_0T_2$ | 1976.3 | 4.399 | 6.479 |
| $_0T_3$ | 1266.1 | 4.856 | 5.594 |
| $_0T_4$ | 957.3 | 4.974 | 5.205 |
| $_0T_5$ | 778.6 | 4.994 | 4.974 |
| $_0T_6$ | 660.1 | 4.979 | 4.827 |
| $_0T_7$ | 574.8 | 4.951 | 4.730 |
| $_0T_8$ | 510.0 | 4.921 | 4.665 |
| $_0T_9$ | 458.9 | 4.892 | 4.618 |
| $_0T_{10}$ | 417.5 | 4.864 | 4.583 |
| $_0S_2$ | 2742.1 | 3.171 | 4.348 |
| $_0S_3$ | 1721.9 | 3.570 | 4.829 |
| $_0S_4$ | 1217.4 | 3.912 | 5.289 |
| $_0S_5$ | 929.2 | 4.185 | 5.469 |
| $_0S_6$ | 749.6 | 4.384 | 5.440 |
| $_0S_7$ | 630.6 | 4.513 | 5.225 |
| $_0S_8$ | 548.5 | 4.576 | 4.845 |
| $_0S_9$ | 489.9 | 4.582 | 4.434 |
| $_0S_{10}$ | 446.0 | 4.553 | 4.149 |

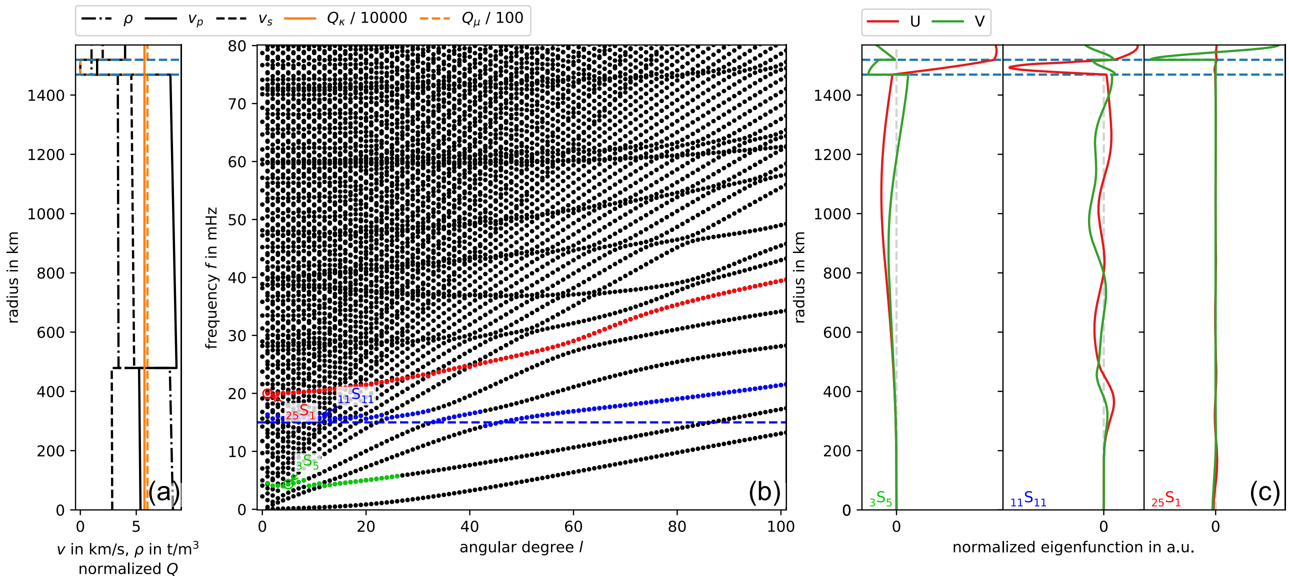


**Figure 12.** Normal mode seismology on Europa. (a) Radially symmetric model of the Jovian moon Europa with 50 km ice thickness over a fluid ocean. (b) Spheroidal mode spectrum based on the cowling approximation, since the size of the moon is small this is appropriate as gravity forces are small, and using attenuation. The horizontal dotted green, blue and red points indicate the flexural, ocean resonance, and Crary model pseudo branches, respectively. The blue dashed line indicates the frequency of the vertical fluid resonance branch when approximated as a simple vertical cavity resonator according to eq. (28). (c) Spheroidal mode eigenfunctions for the modes indicated in the (b): $_3S_5$ (flexural mode), $_{11}S_{11}$ (ocean resonance mode), $_{25}S_1$ (Crary mode). See main text for details.

modified version of the interior structure model of Panning *et al.* (2017). The model, which is shown in Fig. 12(a), consists of a 50-km thick ice layer atop a 50-km thick water layer. The mantle consists of rocky silicate material, whereas the core is considered to be Fe-rich and solid.

A planetary body with a decoupled ice-covered surface is, from a seismic perspective, an interesting object because it gives rise to evanescent seismic phases that predominantly excite the ice sheet. These seismic phases are called Crary and flexural waves (Crary 1954). Crary waves are resonant SV waves in the ice sheet produced by multiple reflections at the boundaries. Hence, their resonance frequency depends strongly on the thickness of the ice sheet. Flexural waves are a predominantly vertical motion of the ice as a whole. Consequently, studying the interior of Europa is probably best undertaken through detection and analysis of seismic surface waves (Kovach & Chyba 2001; Panning *et al.* 2006).

Because of the small mass of the moon, there is little difference in normal mode spectra between full gravity and Cowling. Hence, we use the Cowling approximation for the computations performed here. Resultant low-frequency spheroidal modes for Europa are shown in Fig. 12(b), up to a frequency of 80 mHz and an angular degree of 100.

In contrast to the terrestrial and Martian spectra shown earlier, Europa modes also include flexural and Crary modes that are exemplary of modes that are trapped in the ice sheet. For the three modes marked in green, blue and red in Fig. 12(b), we show the corresponding eigenfunctions in Fig. 12(c): ${}_3S_5$ represents a flexural mode; ${}_{11}S_{11}$ illustrates an ocean resonance mode; while ${}_{25}S_1$ indicates a Crary mode. We further identify flexural (green dotted lines), water resonance (blue dotted lines) and Crary (red dotted line) pseudo-branches.

The fundamental flexural pseudo-branch (green dotted line) in the spectrum shows a similar structure as the Crary pseudo-branch. We also identify a vertical fluid resonance branch (blue dotted line). The frequency $f$ of this vertical fluid resonance branch can, assuming a simple vertical cavity resonator, be approximately estimated from

$$f(\tilde{n}) = \frac{(\tilde{n}+1)\mathrm{V_P}}{2d}, \tag{28}$$

where $\tilde{n}$ is the mode number and $d$ is ocean thickness. For the case of a 50-km-thick fluid layer and a $P$-wave velocity of $V_P = 1.5\ \mathrm{km\,s^{-1}}$, a frequency $f = 15.0$ mHz is obtained for $\tilde{n} = 0$, which is indicated by the horizontal blue dashed line in Fig. 12(b). This value is seen to be in good agreement with the value obtained from superposition of the vertical fluid resonance branch (blue dotted line). Generally, the various branches do not follow the overtone branches strictly, but at times instead consist of multiple overtones, which in superposition will give rise to flexural, vertical fluid resonance and Crary phases in a seismogram.

## 5 DISCUSSION AND CONCLUSION

In this work, we have used the spectral element method to build the software package `specnm` for the generation of normal mode spectra of spherically symmetric bodies. One of the main motivations for this approach was to avoid the potentially unstable mode counting based on zero crossings of the characteristic function (Woodhouse 1988) that is required in classical methods to ensure all eigenfrequencies are found. While we succeeded in this goal, the eigenfunctions are computed directly in the matrix-based approach and not as a linear combination of fundamental solutions. The characteristic function, computed from the fundamental solutions and used for mode counting, is therefore not accessible. As a potential drawback, the overtone number of a given mode can thus not be obtained from the mode itself, but only indirectly from its location in the spectrum.

Nevertheless, we are confident that the versatility, simplicity and accuracy of `specnm`, will be of benefit to the community and we publish it alongside this study in open source format.

Future developments in normal mode seismology will include the development of 3-D long-period numerical time simulations, in which `specnm` may be used as a tool for setting limits on the frequency range for which a full gravity implementation will be needed (van Driel *et al.* 2021).

## ACKNOWLEDGEMENTS

A number of colleagues have helped with suggestions for improving the material presented herein: we are grateful to Christian Böhm for informed discussions on eigenvalue problems and Simon Stähler for input on icy-moon seismology. We also thank the editor Andrew Valentine and reviewers David Al-Attar and Yann Capdeville for thoughtful and constructive comments. This work was supported by grants from the Swiss National Science Foundation (projects 159907, 172508, 191892, and 197369), the European Research Council (ERC) under the EU's Horizon 2020 programme (grant No. 714069) and the Swiss National Supercomputing Centre (CSCS) under project ID s922.

## DATA AVAILABILITY

A snapshot of the software as used in this study is available online (DOI:10.5281/zenodo.5711521, Kemper *et al.* 2021).

## REFERENCES

Al-Attar, D., 2007. A solution of the elastodynamic equation in an anelastic earth model, *Geophys. J. Int.,* **171**(2), 755–760.

Al-Attar, D. & Tromp, J., 2013. Sensitivity kernels for viscoelastic loading based on adjoint methods, *Geophys. J. Int.,* **196**(1), 34–77.

Al-Attar, D., Woodhouse, J.H. & Deuss, A., 2012. Calculation of normal mode spectra in laterally heterogeneous earth models using an iterative direct solution method, *Geophys. J. Int.,* **189**(2), 1038–1046.

Alterman, Z., Jarosch, H. & L. Pekeris, C., 1959. Oscillation of the earth, *Proc. R. Soc. Lond., A.,* **252** , doi:10.1098/rspa.1959.0138.

Amestoy, P., Duff, I.S., Koster, J. & L'Excellent, J.-Y., 2001. A fully asynchronous multifrontal solver using distributed dynamic scheduling, *SIAM J. Matrix Anal. Appl.,* **23**(1), 15–41.

Anderson, J., Schubert, G., Jacobson, R., Lau, E., Moore, W. & Sjogren, W., 1998. Europa's differentiated internal structure: Inferences from four galileo encounters, *Science,* **281**(5385), 2019–2022.

Babuška, I. & Osborn, J., 1991. Eigenvalue problems, in *Handbook of Numerical Analysis,* Vol. 2: Finite Element Methods (Part 1), pp. 641–787, Elsevier.

Banerdt, W.B. *et al.*, 2020. Initial results from the insight mission on mars, *Nat. Geosci.,* **13**(3), 183–189.

Bissig, F. *et al.*, 2018. On the detectability and use of normal modes for determining interior structure of mars, *Space Sci. Rev.,* **214**(8), 114 , doi:10.1007/s11214-018-0547-9.

Bolt, B.A. & Derr, J.S., 1969. Free bodily vibrations of the terrestrial planets, *Vistas Astron.,* **11,** 69–102.

Buland, R. & Gilbert, F., 1984. Computation of free oscillations of the earth, *J. Comput. Phys.,* **54**(1), 95–114.

Chaljub, E. & Valette, B., 2004. Spectral element modelling of three-dimensional wave propagation in a self-gravitating earth with an arbitrarily stratified outer core, *Geophys. J. Int.,* **158**(1), 131–141.

Cohen, G.C. & Pernet, S., 2017. *Finite Element and Discontinuous Galerkin Methods for Transient Wave Equations,* Springer.

Cowling, T.G., 1941. The non-radial oscillations of polytropic stars, *Mon. Not. R. astr. Soc.,* **101,** 367.

Crary, A., 1954. Seismic studies on Fletcher's Ice Island, T-3, *EOS, Trans. Am. geophys. Un.,* **35**(2), 293–300.

Dahlen, F. & Tromp, J., 1998. *Theoretical Global Seismology,* Princeton Univ. Press.

Dziewonski, A.M. & Anderson, D.L., 1981. Preliminary reference earth model, *Phys. Earth planet. Inter.,* **25**(4), 297–356.

Frame, D., He, R., Ipsen, I., Lee, D., Lee, D. & Rrapaj, E., 2018. Eigenvector continuation with subspace learning, *Phys. Rev. Lett.,* **121**(3) , doi:10.1103/PhysRevLett.121.032501.

French, S.W. & Romanowicz, B., 2014. Whole-mantle radially anisotropic shear velocity structure from spectral-element waveform tomography, *Geophys. J. Int.,* **199**(3), 1303–1327.

Giardini, D., Li, X.-D. & Woodhouse, J.H., 1987. Three-dimensional structure of the earth from splitting in free-oscillation spectra, *Nature,* **325**(6103), 405–411.

Gudkova, T., Zharkov, V. & Lebedev, S., 1993. Theoretical spectrum of free oscillations of Mars, *Solar Syst. Res.,* **27**(2), 129–148.

Hernandez, V., Roman, J.E. & Vidal, V., 2005. Slepc: a scalable and flexible toolkit for the solution of eigenvalue problems, *ACM Trans. Math. Softw.,* **31**(3), 351–362.

Igel, H., 2017. *Computational Seismology: A Practical Introduction,* Oxford Univ. Press.

Irving, J.C., Cottaar, S. & Lekić, V., 2018. Seismically determined elastic parameters for earth's outer core, *Sci. Adv.,* **4**(6),.

Ishii, M. & Tromp, J., 1999. Normal-mode and free-air gravity constraints on lateral variations in velocity and density of earth's mantle, *Science,* **285**(5431), 1231–1236.

Kemper, J., van Driel, M. & Munch, F., 2021. *specnm: Spectral Element Normal Mode Code,* [Online; accessed 2021-11-18].

Khan, A. *et al.*, 2021. Upper mantle structure of Mars from InSight seismic data, *Science,* **373**(6553), 434–438.

Khan, A., Liebske, C., Rozel, A., Rivoldini, A., Nimmo, F., Connolly, J. A.D., Plesa, A.-C. & Giardini, D., 2018. A geophysical perspective on the bulk composition of Mars, *J. geophys. Res.,* **123**(2), 575–611.

Khurana, K., Kivelson, M., Stevenson, D., Schubert, G., Russell, C., Walker, R. & Polanskey, C., 1998. Induced magnetic fields as evidence for subsurface oceans in Europa and Callisto, *Nature,* **395**(6704), 777–780.

Knapmeyer-Endrun, B. *et al.*, 2021. Thickness and structure of the Martian crust from InSight seismic data, *Science,* **373**(6553), 438–443.

Kovach, R.L. & Chyba, C.F., 2001. Seismic detectability of a subsurface ocean on Europa, *Icarus,* **150**(2), 279–287.

Lamb, H., 1881. On the vibrations of an elastic sphere, *Proc. Lond. Math. Soc.,* **s1–13**(1), 189–212.

Lehoucq, R.B., Sorensen, D.C. & Yang, C., 1998. *ARPACK Users' Guide: Solution of Large-Scale Eigenvalue Problems with Implicitly Restarted Arnoldi Methods,* Vol. **6,** SIAM.

Lei, W. *et al.*, 2020. Global adjoint tomography—model GLAD-M25, *Geophys. J. Int.,* **223**(1), 1–21.

Lognonné, P., 1991. Normal modes and seismograms in an anelastic rotating earth, *J. geophys. Res.,* **96**(B12), 20 309–20 319.

Lognonné, P., Beyneix, J.G., Banerdt, W.B., Cacho, S., Karczewski, J.F. & Morand, M., 1996. Ultra broad band seismology on intermarsnet, *Planet. Space Sci.,* **44**(11), 1237–1249.

Masters, G., Woodhouse, J. & Freeman, G., 2011. *Mineos v1.0.2,* [software].

Nissen-Meyer, T., Fournier, A. & Dahlen, F.A., 2007. A two-dimensional spectral-element method for computing spherical-earth seismograms–i. moment-tensor source, *Geophys. J. Int.,* **168**(3), 1067–1092.

Nissen-Meyer, T., van Driel, M., Stähler, S.C., Hosseini, K., Hempel, S., Auer, L., Colombi, A. & Fournier, A., 2014. Axisem: broadband 3-d seismic wavefields in axisymmetric media, *Solid Earth,* **5**(1), 425–445.

Nolet, G., 2008. *A Breviary of Seismic Tomography: Imaging the Interior of the Earth and Sun,* Cambridge Univ. Press.

Okal, E.A. & Anderson, D.L., 1978. Theoretical models for mars and their seismic properties, *Icarus,* **33**(3), 514–528.

Panning, M., Lekic, V., Manga, M., Cammarano, F. & Romanowicz, B., 2006. Long-period seismology on Europa: 2. Predicted seismic response, *J. geophys. Res.,* **111**(E12), doi:10.1029/2006JE002712.

Panning, M.P. *et al.*, 2017. Planned products of the Mars structure service for the insight mission to Mars, *Space Sci. Rev.,* **211**(1-4), 611–650.

Park, J.J., 1986. Synthetic seismograms from coupled free oscillations: effects of lateral structure and rotation, *J. geophys. Res.,* **91**(B6), 6441 , doi:10.1029/JB091iB06p06441.

Poisson, S., 1829. Mémoire sur l'équilibre et le Mouvement des Corps élastiques, *Mémoires l'Académie R. des Sci. l'Institut Fr.,* **8,** 357–570.

Resovsky, J.S. & Ritzwoller, M.H., 1999. Regularization uncertainty in density models estimated from normal mode data, *Geophys. Res. Lett.,* **26**(15), 2319–2322.

Scott, D., 1982. The advantages of inverted operators in Rayleigh–Ritz approximations, *SIAM J. Scient. Stat. Comput.,* **3**(1), 68–75.

Simmons, N.A., Myers, S.C., Morency, C., Chiang, A. & Knapp, D.R., 2021. SPiRaL: a multi-resolution global tomography model of seismic wave speeds and radial anisotropy variations in the crust and mantle, *Geophys. J. Int.,* **227**(2), 1366–1391.

Slichter, L.B., 1961. THE FUNDAMENTAL FREE MODE OF THE EARTH'S INNER, *Proc. Natl. Acad. Sci. U.S.A,* **47**(), 186.

Snieder, R. & Sens-Schönfelder, C., 2021. Local coupling and conversion of surface waves due to Earth's rotation. Part 1: theory, *Geophys. J. Int.,* **225**(1), 158–175.

Stähler, S.C. *et al.*, 2021. Seismic detection of the Martian core, *Science,* **373**(6553), 443–448.

Stähler, S.C., Panning, M.P. Vance, S.D. Lorenz, R.D. van Driel, M. Nissen-Meyer, T. & Keder, S. 2018. Seismic wave propagation in icy ocean worlds, *J. geophys. Res.,* **123**(), 206–232.

Stoneley, R., 1924. Elastic waves at the surface of separation of two solids, *Proc. R. Soc. London, Ser. A, Containing Papers of a Mathematical and Physical Character,* **106**(), 416–428.

Takeuchi, H. & Saito, M., 1972. Seismic surface waves, *Methods Comput. Phys.,* **11,** 217–295.

Thomson, W., 1863. On the rigidity of the Earth, *Phil. Trans. R. Soc. Lond.,* **153,** 573–582.

Trampert, J., Deschamps, F., Resovsky, J. & Yuen, D., 2004. Probabilistic tomography maps chemical heterogeneities throughout the lower mantle, *Science,* **306**(5697), 853–856.

Tromp, J. & Dahlen, F.A., 1990. Free oscillations of a spherical anelastic earth, *Geophys. J. Int.,* **103**(3), 707–723.

Valette, B., 1987. Spectre des oscillations libres de la Terre: aspects mathématiques et géophysiques, *PhD thesis*, Paris 6.

van Driel, M., Kemper, J. & Boehm, C., 2021. On the modeling of self-gravitation for full 3D global seismic wave propagation, *Geophys. J. Int.,* **227**(1), 632–643.

Vance, S.D. *et al.*, 2018. Geophysical investigations of habitability in ice-covered ocean worlds, *J. geophys. Res.,* **123**(1), 180–205.

Wiggins, R.A., 1976. A fast, new computational algorithm for free oscillations and surface waves, *Geophys. J. Int.,* **47**(1), 135–150.

Woodhouse, J., 1988. The calculation of the eigenfrequencies and eigenfunctions of the free oscillations of the earth and sun, in *Seismological Algorithms: Computational Methods And Computer Programs,* pp. 321–370, ed. Doornbos, D.J., Academic Press.

Woodhouse, J. & Deuss, A., 2015. Earth's free oscillations, in *Treatise on Geophysics,* 2nd edn, pp. 79–115, ed. Schubert, G., Elsevier.

Woodhouse, J.H. & Dziewonski, A.M., 1984. Mapping the upper mantle: three-dimensional modeling of earth structure by inversion of seismic waveforms, *J. geophys. Res.,* **89**(B7), 5953–5986.

Zábranová, E., Hanyk, L. & Matyska, C., 2017. Matrix eigenvalue method for free-oscillations modelling of spherical elastic bodies, *Geophys. J. Int.,* **211,** 1254–1271.

Zahnle, K., Dones, L. & Levison, H.F., 1998. Cratering rates on the Galilean satellites, *Icarus,* **136**(2), 202–222.

Zheng, Y., Nimmo, F. & Lay, T., 2015. Seismological implications of a lithospheric low seismic velocity zone in Mars, *Phys. Earth planet. Inter.,* **240,** 132–141.

## APPENDIX A: EQUATIONS FROM THE LITERATURE

This sections includes the equations used in the derivations in the main part of the paper, copied from Dahlen & Tromp (1998) for completeness. Toroidal first order equations:

$$\partial_r W = r^{-1}W + L^{-1}T, \tag{A1}$$

$$\partial_r T = [-\omega^2\rho + (k^2-2)Nr^{-2}]W - 3r^{-1}T. \tag{A2}$$

Spheroidal first order equations:

$$\partial_r U = -2C^{-1}Fr^{-1}U + kC^{-1}Fr^{-1}V + C^{-1}R, \tag{A3}$$

$$\partial_r V = -kr^{-1}U + r^{-1}V + L^{-1}S, \tag{A4}$$

$$\partial_r P = -4\pi G\rho U - (l+1)r^{-1}P + B, \tag{A5}$$

$$\begin{aligned}\partial_r R = {} & [-\omega^2\rho - 4\rho g r^{-1} + 4(A - N - C^{-1}F^2)r^{-1}]U + [k\rho g r^{-1} - 2k(A - N - C^{-1}F^2)r^{-2}]V - (l+1)\rho r^{-1}P \\ & -2(1 - C^{-1}F)r^{-1}T_U + kr^{-1}T_V + \rho T_P,\end{aligned} \tag{A6}$$

$$\begin{aligned}\partial_r S = {} & [k\rho g r^{-1} - 2k(A - N - C^{-1}F^2)r^{-2}]U - [\omega^2\rho + 2Nr^{-2} - k^2(A - C^{-1}F^2)r^{-2}]V + k\rho r^{-1}P \\ & -kC^{-1}Fr^{-1}T_U - 3r^{-1}T_V,\end{aligned} \tag{A7}$$

$$\partial_r B = -4\pi G(l+1)\rho r^{-1}U + 4\pi Gk\rho r^{-1}V + (l-1)r^{-1}T_P. \tag{A8}$$

## APPENDIX B: WEAK FORM OF THE RADIAL ODEs

This section includes some additional derivations and equations for the symmetric weak form as described in the main part of the paper. Radial equation with eigenfunction $U(r)$ and its test function $\tilde{U}(r)$. The included traction $T_U(V=0)$ is the same as for spheroidal modes setting the $V$ eigenfunction to zero:

$$\begin{aligned}\omega^2\int_\Omega \rho U\tilde{U}r^2\,\mathrm{d}r = {} & -\left[T_U(V=0)\tilde{U}r^2\right]_0^{r_\mathrm{surf}} + \left[T_U(V=0)\tilde{U}r^2\right]_-^+ \\ & + \int_\Omega Cr^2\partial_r U\partial_r\tilde{U}\,\mathrm{d}r + \int_\Omega 2Fr(U\partial_r\tilde{U} + \partial_r U\tilde{U})\,\mathrm{d}r + \int_\Omega [4(A-N) - 4\rho g r]U\tilde{U}\,\mathrm{d}r.\end{aligned} \tag{B1}$$

Full gravity spheroidal equation with eigenfunctions $U(r)$, $V(r)$, $P(r)$ and its symmetric counterparts $\tilde{U}(r)$, $\tilde{V}(r)$, $\tilde{P}(r)$:

$$\begin{aligned}\omega^2\int_\Omega \rho(U\tilde{U} + V\tilde{V})r^2\,\mathrm{d}r = {} & -\left[T_U\tilde{U}r^2\right]_0^{r_\mathrm{surf}} - \left[T_V\tilde{V}r^2\right]_0^{r_\mathrm{surf}} - \left[T_P\tilde{P}r^2\right]_0^{r_\mathrm{surf}} + \left[T_U\tilde{U}r^2\right]_-^+ + \left[T_V\tilde{V}r^2\right]_-^+ + \left[T_P\tilde{P}r^2\right]_-^+ \\ & + \int_\Omega L(kU - V + r\partial_r V)(k\tilde{U} - \tilde{V} + r\partial_r\tilde{V})\,\mathrm{d}r + \int_\Omega (A-N)(2U - kV)(2\tilde{U} - k\tilde{V})\,\mathrm{d}r \\ & - \int_\Omega Fr[2(\partial_r U\tilde{U} + U\partial_r\tilde{U}) - k(V\partial_r\tilde{U} + \partial_r U\tilde{V})]\,\mathrm{d}r + \int_\Omega \rho g r[-4U\tilde{U} + k(V\tilde{U} + U\tilde{V})]\,\mathrm{d}r \\ & + \int_\Omega Cr^2\partial_r U\partial_r\tilde{U}\,\mathrm{d}r + \int_\Omega N(k^2-2)V\tilde{V}\,\mathrm{d}r + \int_\Omega \rho r^2(\partial_r P\tilde{U} + P\partial_r\tilde{U})\,\mathrm{d}r + \int_\Omega 4\pi G\rho^2 r^2 U\tilde{U}\,\mathrm{d}r \\ & + \int_\Omega k\rho r(P\tilde{V} + V\tilde{P})\,\mathrm{d}r + \int_\Omega (4\pi G)^{-1}r^2\partial_r P\partial_r\tilde{P}\,\mathrm{d}r \\ & + \int_\Omega (l+1)(4\pi G)^{-1}r(P\partial_r\tilde{P} + \partial_r P\tilde{P})\,\mathrm{d}r + \int_\Omega (l+1)^2(4\pi G)^{-1}P\tilde{P}\,\mathrm{d}r\end{aligned} \tag{B2}$$

Note that the left-hand side does not include $P(r)$ or $\tilde{P}(r)$, hence the mass matrix is positive semi definite.